

# NUCLEAR DATA COVARIANCE ANALYSIS OF AN ENERGY TUNING ASSEMBLY FOR SIMULATING NUCLEAR WEAPON ENVIRONMENTS

## 1. Introduction

### 1.1 Motivation

Nuclear deterrence is the cornerstone of U.S. nuclear policy and strategy [2]. A key component of deterrence theory that enables U.S. strategic objectives is the credibility of the nuclear capability. Two key attributes related to nuclear deterrence credibility are attribution capabilities to hold potential threats accountable and the surety of nuclear weapon systems to function if needed.

The final full scale U.S. nuclear weapon testing was performed on 23 September, 1992. The non-proliferation of nuclear weapons and general health and environmental concerns from the radioactive emissions were key drivers for eliminating testing of any kind. The Comprehensive Test-Ban Treaty (CTBT) banned nuclear explosions for all signatories or supporting nations for an indefinite duration since 1996. A handful of tests have been conducted after the CTBT's effective date; none have been by the U.S.

However, there is still a need for the capabilities previously provided through nuclear testing for the study of nuclear environments to support the credibility of the nuclear deterren<sup>ce</sup>. Previous work has shown that the loss of nuclear testing has created a capability gap to reproduce nuclear weapon environments of interest to national security applications including nuclear weapons effects (NWE) and TNF [3, 4].

### 1.1.1 Nuclear Weapon Certification Capability Gap

Each U.S. administration has supported the requirement and maintenance of a nuclear force structure after the elimination of nuclear tests. President Donald Trump stated at the 2018 State of the Union Address, “As part of our defense, we must modernize and rebuild our nuclear arsenal, hopefully never having to use it, but making it so strong and powerful that it will deter any acts of aggression” [5]. The National Nuclear Security Administration (NNSA) is tasked with the mission of maintaining the nuclear stockpile’s safety, security, and effectiveness under the Stockpile Stewardship Program (SSP).

Testing in relevant environments is generally recognized as a critical requirement for nuclear weapon certification, just as it is for any Department of Defense (DOD), weapon system. Actual system tests cannot be performed, so demonstration of components or subsystems in a the relevant environment is an import part of the technology readiness level as part of the DOD Instruction 5000.02 series [6]. Additionally, the DOD nuclear certification process is derived from DOD Directive 3150.02 [7]. Representative nuclear weapons system and effects testing supporting SSP is carried out by the Department of Energy (DOE), DOD, national laboratories, and supporting organizations. The scope of the testing sites is incredibly wide, ranging from radio frequency communications to the prompt gamma and neutron emissions following a nuclear event. Some testing is conducted on components of the nuclear weapons themselves, such as the near-system-level hydrodynamic tests performed with inert pits [8]. However, many aspects of nuclear weapons ~~are only available for testing via computational methods or small-scale experiments~~, which may not truly represent the physics involved in a nuclear weapon.

One of the larger identified gaps for testing is neutron environments available at current facilities in comparison with the environment that a nuclear weapon would

see or produce [3]. The current neutron sources do not have an accurate energy or temporal distribution for the nuclear environment that nuclear systems are required to survive in certification testing. This problem is complicated further as the transmitted neutron flux through the physical environment and to the target varies significantly in energy and temporal distribution depending on the scenario and system being considered. The lack of a relevant facility has led to a reliance on simulations and large engineering safety factors [9]. To address this capability gap, it would be beneficial to have a testing capability with an accurate energy and temporal profile.

### 1.1.2 Technical Nuclear Forensics Capability Gap

A key strategy under countering nuclear terrorism in the 2018 Nuclear Posture Review affirmed the importance of “deterring state support for nuclear terrorism through advanced forensics and attribution capabilities” [2]. To this end, the technical nuclear forensics (TNF) community requires the ability to generate representative post-detonation debris samples for training and development of attribution techniques. The generation of accurate fission product inventories in the representative debris is both extremely important for the attribution of the origin of a nuclear device and very difficult to do with existing facilities due to a diminishing pool of subject matter experts and outdated facilities [10].

According to the Joint Nuclear Forensics Working Group report from 2013,

Current post-detonation debris analysis techniques derive largely from the nuclear weapons test programs of the Cold War. Leveraging the Cold War infrastructure enabled a baseline forensics capability to be established quickly, but has resulted in a capability that relies largely on science and technology developed in the nuclear-testing era, with timelines and priorities sometimes distinct from those of nuclear forensics. In addition, current analysis methods are often labor-intensive, and rely on education and training that are no longer prominent in the U.S. university system [11].

Advances in attribution capabilities for TNF require facilities that produce nuclear weapon relevant environments which drives the distribution of observed fission products. The attribution problem is also complex in that chemical and physical processes post-detonation can drastically impact the debris. The generation of synthetic weapons debris would be of enormous benefit to the TNF community for training purposes. Furthermore, the ability to generate spectrally accurate fission products is of great use for attribution capabilities.

Post-detonation fission product analysis provides a means of determining many characteristics of a nuclear device. In particular, according to a US National Research Council report from 2009, the fission debris can provide the most accurate measurement of weapon yield when combined with device information [12]. From an attribution standpoint, the CTBT utilizes fission products to verify compliance with the nuclear test ban [13]. Numerous fission products are of great importance for varying aspects of nuclear sciences. A couple notable examples are  $^{90}\text{Sr}$  and  $^{14}\text{C}$  which used for estimating dosage received from past nuclear weapons testing [14].

### 1.1.3 Neutron Environment Capability Gaps

The capability gaps outlined for nuclear weapons certification and TNF motivate the need to generate spectrally accurate nuclear weapon neutron environments. In particular, the present testing capability does not have the ability to produce neutron spectra that combine a thermonuclear (TN) and prompt fission neutron spectrum (PFNS). The vast majority of testing facilities are focused on the Watt-fission spectrum, while a few are capable of producing the 14.1 MeV TN component from the deuterium-tritium (DT) fusion process [15]. Several examples of testing facilities for prompt neutrons outlined in Table 1 are the Sandia Pulsed Reactor III (SPR), Sandia Annual Core Research Reactor (ACCR), White Sands Missile Range (WSMR) Fast

Burst Reactor (FBR), the Los Alamos National Laboratory (LANL) Rotating Target Neutron Source (RTNS), and the LANL Weapons Neutron Research facility (WNR). The differential spectral profile of these sources compared to a notional TN+PFNS is shown in Figure 1.

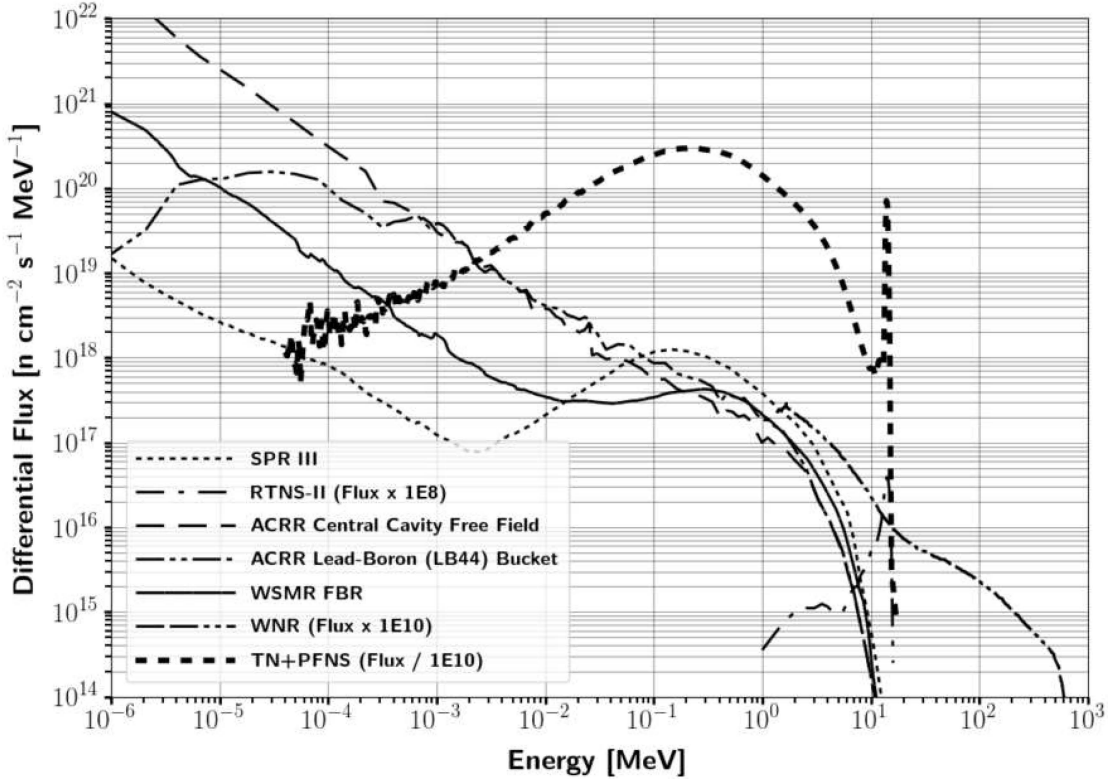


**Figure 1. Comparison of selected neutron sources to notional TN+PFNS [4].**

Each of the available neutron sources has an important purpose for national security applications; however, they cannot meet the energy and temporal spectrum for every nuclear testing requirement. In comparison with the TN+PFNS, nearly all of the neutron sources are heavily weighted to lower energies and do not contain enough high energy neutrons for the TN component. The RTNS has a high energy component, but the magnitude of the flux is substantially lower than required for some applications. The temporal aspect of the neutron flux also does not generally match to a nuclear weapon spectrum for some available facilities. Additionally, these

large facilities are often at risk for shutdown, such as the SPR-III decommissioning for storage at the Nevada Test Site in late 2006 [16]. Many of these facilities are discussed for shutdown with growing regulatory demands and security requirements for storing highly enriched uranium (HEU) [7]. Gathering accurate experimental results requires a neutron flux spectrum equivalent to that of a true nuclear event, which creates a need for a neutron source capable of emulating the environment. Therefore, development of a TN+PFNS source would enable production of the correct fission product inventory in surrogate debris and thereby enhance the ability of the TNF community to perform the attribution mission. Additionally, a TN+PFNS source capable of NWE testing would greatly improve the nuclear weapon certification process.

## 1.2 Background

Many approaches can be used to create nuclear weapon relevant neutron spectra in the absence of full-scale nuclear weapons testing. Some mechanisms are more applicable within different communities in nuclear sciences. Four main possible ways that the neutron environments are approximated for synthetic fission product debris production are sample doping, direct production using fission converters, surrogate methods, and spectral modification of existing sources [4]. In the context of neutron effects on electronics, the key approaches utilized are using existing sources, computational models, and surrogate charged particle reactions. Each of these methods are limited in representing the neutron environment experienced in a nuclear weapon.

The sample doping technique is accomplished by selectively correcting mass chains to modeled equivalent ratios. The resultant sample is built so as to look like it was produced with a desired energy dependent fluence. A somewhat common TNF application using sample doping is the production of glass surrogate fallout debris for

use in exercises or training [18]. The glassy matrix is created to emulate the solidified fission debris and entrained environment that is swept up in the stem of a nuclear explosion. The glass is doped with uranium and irradiated under various neutron environments depending on the requirements; however, the irradiation often done with a thermal neutron reactor. A key deficiency with utilizing a thermal reactor is that the neutron energy spectrum is not a close approximation to a weapon spectrum, and the fission products that follow will therefore not be either. Utilizing a harder, or higher energy, neutron spectrum reactor is a better approximation; however, it is still not an accurate representation. Additionally, the sample doping technique can be approached by irradiating different samples at different facilities. A final sample which has the “correct” fission product ratios can be created by selectively pulling mass chains from the irradiated samples. This sample doping technique creates a fission product debris sample; however, the spectral and temporal nature of the sample is not equivalent to what would be produced in a real nuclear explosion.

Direct conversion utilizes nuclear reactions to create a shaped neutron flux, which can be done via charged particle interactions or through fusion sources with a fission converter. It has been shown that direct production is “impractical, complex, and unlikely to be implemented for safety or technological limitations” [4].

Surrogate methods rely on the formation of an equivalent compound nucleus through an alternative reaction mechanism [19, 20]. Surrogate methods are popular in studies where forming the product nucleus through the desired reaction is difficult or the energy cannot be fine-tuned. An example of this is neutron induced fission on U-235 where a possible surrogate for U-235 neutron induced fission reaction, ( $n,f$ ), is Th-232 ( $\alpha,f$ ), both of which form the U-236 compound nucleus. The surrogate approach has seen success; however, the nuclear data supporting the reactions is not as well understood [21, 22]. Additionally, there are some assumptions on the

compound nuclear equilibration and spin-parity state which can impact the decay channels of the studied reactions [19].

Another commonly used surrogate method is to utilize charged particles for neutron damage in radiation effects on electronics. Ion beams can be used as a surrogate for neutrons by comparing the relative displacements per atom caused by the charged particle compared to a neutron [23]. A major benefit of using ion beams is that the energy can be finely tuned both in energy and deposition location, whereas neutrons are not as easily controlled. A disadvantage of using charged particles is that a large portion of the energy deposition as it travels through materials is based on electronic stopping power, while the neutral neutrons have negligible electronic interactions. The Qualification Alternatives to the Sandia Pulsed Reactor (QASPR) program is the most significant venture into the use of surrogate ions to perform neutron effects component level testing as a replacement alternative for the SPR [3]. QASPR combines operational irradiation facilities with modeling to predict neutron effects. While there have been substantial improvements to increasing the verification and validation of simulated data to experimental outcomes, the validation for the experimental data benchmarked to neutron experimental data is lacking in many cases [24].

The final approach that could be used is spectral modification, a method of altering a neutron spectrum through nuclear interactions to generate an energy spectrum of interest. Fundamentally, spectral modification is the goal of water moderated nuclear reactors to increase efficiency and allow the use of low enriched fuel.

Spectral modification is also performed in beam shaping assemblies used for boron neutron capture therapy (BCNT), where neutrons are used to treat tumors through neutron capture reactions in boron. A somewhat optimized objective neutron spectrum focused on the epithermal region is published by the International Atomic Energy Agency (IAEA) [25]. BCNT has been explored with a wide vari-

ety of sources including accelerators and deuterium-deuterium (DD) fusion. A beam shaping assembly can be designed to moderate a source neutron flux to appropriate thermal, epithermal, and fast spectrum for BCNT [26]. The build up of a design is produced primarily through moderation, reflection, and collimation of neutrons to the patient [27]. However, the approach to designing a beam shaping assembly lends itself to inefficiencies from an energy and population perspective. The collimation process blocks out a portion of potentially usable particles. Additionally, the beam shaping assembly resultant spectrum is often under-optimized. The development process could be enhanced to increase efficiency and spectral profile agreement with the objectives.

A novel spectral modification approach was developed by the University of California-Berkeley and Lawrence Livermore National Laboratory (LLNL) for the development of an energy tuning assembly (ETA) to modify the National Ignition Facility (NIF) source to produce a TN+PFNS [4]. To perform the spectral modification, the Coeus metaheuristic optimization software package was developed to avoid manpower intensive iterative studies and enable the rapid design of future ETAs to convert a facility’s characteristic source spectrum to any arbitrary objective spectrum, within the constraints of physics [28]. Gnowee, the Coeus optimization engine, was developed for “rapid convergence to nearly globally optimum solutions” of this class of engineering problems [29]. It is important to note that the Gnowee and Coeus codes have applicability over a wide range of engineering problems, not just for the production of a TN+PFNS.

The result of the ETA design produced an acceptable representation of the TN+PFNS with the associated fission product distribution. The ETA design has been built and preliminary validation tests were conducted at the Lawrence Berkeley National Laboratorys 88-Inch Cyclotron [4, 30]. The preliminary validation utilized 33 MeV

deuterium breakup on tantalum as a neutron source and investigated the ability to model the ETA performance [30]. Integral validation is planned in fiscal year (FY) 2019, and a development shot to enhance ETA performance is planned in FY2020.

### 1.3 Problem

~~The previous work made great progress; however, there are several deficiencies that need to be addressed.~~ The broad research objective for this work is *Can an accurate neutron energy distribution expected from a "typical" thermonuclear or boosted nuclear weapon detonation be produced using spectral modification at the NIF?* This research effort aims to address three main problem areas for ETA and spectral shaping of neutron sources for simulating nuclear weapon environments that were raised by previous work. Additionally, ETA needs to be characterized as a potential ‘short pulse’ neutron source (SPNS). Each are detailed below along with accompanying research objectives.

1. FY 2019 NIF shot (ETA): Systematic uncertainty is not fully addressed in the previous ETA calculations
  - Quantify the impact of nuclear data covariances of the simulated results for the neutron energy spectrum, foil activation rates, and fission product production rates
  - Design a foil activation diagnostic pack to provide better resolution in the epi-thermal neutron energy range
  - Prioritize and estimate production of fission products for radio-chemical analysis using recently published data
2. The ETA at NIF was not evaluated for use as a SPNS

- Model the neutron timing profile and expected flux in the ETA experimental cavity

## 1.4 Questions and Hypothesis

The research questions and hypotheses associated with the problems outlined in Section 1.3 are detailed below. They are organized by the problem and capability that they support.

### 1. 2019 ETA Fission Product Production Experiment

- **What is the impact of nuclear data covariance on the simulated results?** It is expected that including nuclear data uncertainty will increase the relative error by approximately 1% for integrated and well understood reactions and may extend over 10% for less studied reactions thereby dominating Monte Carlo statistical uncertainty.
- **Does the activation foil pack have sufficient coverage of the neutron spectrum to be used for unfolding?** Previous work indicated that the current foil pack design has poor coverage in the epithermal region and is not sufficient to robustly unfold the neutron spectrum should the model deviate from experimental results. Incorporation of better foil characteristics will improve this deficiency, and the performance can be tested through unfolding the ETA generated neutron spectrum using perturbed samples generated from including the nuclear data uncertainty.

### 2. ETA SPNS Characterization

- **Can an ETA be useful as a capability for testing of prompt neutron environments?** It is anticipated that ETA can provide a TN+PFNS

electronic testing capability due to the short NIF neutron pulse ( $\sim 300$  ps), although the sample cavity is smaller than would be required for larger component testing.

## 1.5 Assumptions and Limitations

An omnipresent limitation in many studies of science and engineering is the quality and quantity of available data for applications. Nuclear engineering commonly draws from published works containing the relevant nuclear data and the uncertainties behind them. There is also uncertainty in the published uncertainties as much of the available data is derived from models and never directly tested. The results presented are limited by the currently accepted understanding of nuclear physics phenomena and by the limitations of published data that is consistently being improved upon by the nuclear science community.

The second limitation, which is done so for convenience and publishing ability, is that the nuclear weapon environments are presented at an unclassified level. All information used to develop the neutron flux and profile is available in open literature or derived from unclassified information to produce a representative environment. The accuracy of the representative neutron environment compared to a specific real-world nuclear weapon scenario was not analyzed and will not be presented. The scope of this work aims to provide a position where, if desired, one could easily ~~go from the unclassified spectrum to one that fully meets a requirement~~.

An assumption for this work is the choice of the NIF as the neutron source. Other sources may be present that would also perform the role, but NIF has unique benefits such as the prompt nature of the neutron yield and the fast neutrons arising from DT fusion. Although the NIF has been in operation since approximately 2010, there is a potential insertion of systematic error based on the source characterization and

variability in the source output.

Nuclear weapons can be categorized into three general classes: fission, boosted and TN [15, 31]. It has been shown that the majority of the present capability to produce synthetic debris is most focused on the fission devices [4]. The TN+PFNS was chosen in previous work because it is an area that lacks substantial source development. It is important to note that there is not just one spectrum that can classify the TN+PFNS. The TN portion of the weapon spectrum is assumed to be pure DT fusion [31]. The impact of weapon design, which can vary substantially and play a large role in the resultant neutron energy spectrum, is not evaluated in this work. 

Some physical phenomena present in a true nuclear event are not taken into consideration for this analysis. First, the temperatures seen in nuclear weapons are on the order of  $10^7$  K, which is not feasible for the experiment [32]. Second, the time dependency of the internal neutron flux as the weapon is configured is not taken into account. Additionally, there will be large changes to the flux from initiation to burnout; this work only considers a time and volume average result. Third, the synthetic weapon debris is created without induced fractionation. Chemical fractionation occurs when the nuclear debris formed solidifies based on the condensation point of the constituent materials. It is feasible to perform some level of fractionation; however, the levels of refractories and volatiles will not be altered in this work. 

## 1.6 Approach

The spectral shaping problem is defined by the objectives and constraints. For this research, the problem objectives are the ETA spectrum for fission product generation. The problem constraints are based on the NIF source term and mechanical envelope. The input objectives and constraints were utilized in Coeus to produce a nearly-globally optimum solution for an ETA [4]. The constraints for the problem

are governed by the NIF source which is modeled as the polar direct drive exploding pusher (PDXP), stay-out angle defined by the incident lasers to drive the fusion, and the constraints of the NIF Target and Diagnostic Manipulator (TANDM). The work performed previously has completed a baseline design for the original ETA that will be used for analysis of the expected experimental performance.

The point design is modeled with MCNP5, MCNP6, and SCALE version 6.2 to perform neutron radiation transport. MCNP is used for continuous energy solution, while SCALE is used for group-wise covariance analysis. Additional post-processing is used to incorporate nuclear data uncertainty associated with the activation cross-sections. MCNP versions 5 and 6 are both used depending on compatibility with surface source read (SSR) files generated by LLNL for a full NIF model simulation to account for “room return” and scattering off ancillary equipment. Utilizing two different radiation transport models also increases the degree of confidence in the results. The radiation transport simulations provide results for the reaction rates for foil activation, neutron energy spectra, and temporal aspect of the neutron flux.

The General Description of Fission Observables (GEF) code is utilized for developing the expected fission product yields. GEF is a Monte Carlo and theory based approach that incorporates experimental data to determine fission observables, such as fission product yields [33]. Empirical methods for determining fission product distributions also exist. A formulation of this fit by S. Nagy is also used and is beneficial for comparison to GEF in addition to providing unique isotope yields [34]. These empirical methods often include simplifications, such as ignoring neutron multiplicity, to create a simpler equation and more direct tie to existing data - both a benefit and limitation of this approach.

A foil pack designed to be placed in the ETA experimental cavity will be created to be able to successfully unfold the incident neutron spectra from the activation

foils. The activation foils are selected with many important factors including the confidence in the nuclear data and energy range covered. The modeled foil activities are used with the underlying nuclear data to unfold the neutron spectrum using Pacific Northwest National Laboratory (PNNL) STAYSL. STAYSL relies on least-squares spectral adjustment based on the chi-squared of the measured activities to determine the incident neutron flux [35].

## 1.7 Innovations

This research advances the field of nuclear science and engineering in a few key ways:

1. **Demonstrated further abilities to incorporate nuclear data covariance into fixed radiation transport simulations:** The standard methodology for determining nuclear data uncertainty from stochastic sampling approaches is discussed in Chapters 2 and 3. This work utilized an approach to encompass the full range of uncertainty on the nuclear reactions when sampling from a multivariate normal distribution thereby generating a more accurate depiction of the resultant uncertainty.
2. **Improved the ability to generate synthetic fission product debris:** A major goal of this research is to provide an improvement in spectrally accurate fission product debris production and improve the ability to model the production and predict the resulting debris 
3. **Advanced the field of neutron spectral shaping for radiation effects testing simulators:** The ETA design characterization represents a stepping stone in nuclear certification testing for providing a time- and energy-representative neutron environment.

- 4. Developed methodology for quantifying the neutron flux uncertainty for foil activation unfolding of neutron energy spectra:** The techniques to map the systematic nuclear data uncertainty to an arbitrary group structure are discussed in Chapter3.
- 5. Contribution to future improvements to SCALE:** Various pieces of feedback were provided to Oak Ridge National Laboratory (ORNL) for future improvements to the SCALE package including inconsistent uncertainties from published data, the need for parallelization in individual Monte Carlo simulations, and the need for a high energy group structure with covariance data.

## 2. Theory

This chapter outlines the major nuclear science and engineering theory relevant to spectral shaping and analysis of ETA. First, the basic neutron interaction theory that impacts the ability of a source to be shaped into an objective spectrum is discussed. Next, the nuclear fission process is outlined with a primary focus on fission product generation. After, fundamental aspects of nuclear data and their application in Monte Carlo neutron transport codes and an associated stochastic sampling approach utilizing nuclear data covariance matrices are outlined. Finally, neutron activation foil theory relevant to the unfolding of a neutron spectrum is examined.

### 2.1 Neutron Interactions with Matter

Neutron interaction mechanisms with matter serve as a physical constraint to spectral shaping of a neutron flux spectrum. Neutron interactions can act to moderate, absorb, or even emit more neutrons. The major reaction mechanisms available in the range of the fast to thermal energies that are relevant to nuclear weapon environments are elastic scattering, inelastic scattering, radiative capture, and the release of ‘x’ particle ( $n,xn$ ) reactions. Fission reactions are an extremely important reaction mechanism for the formation of synthetic weapon debris; however, fission does not contribute largely to the spectral modification problem for this application. A diagram summarizing the important neutron reactions is shown in Figure 2.

The neutron interaction probability is described by the neutron microscopic reaction cross-section ( $\sigma_{rxn}$ ), which is a function of the target isotope and incident neutron energy ( $E_n$ ). The microscopic cross-section multiplied by the atomic number density,  $N$ , provides macroscopic cross-section ( $\Sigma_{rxn}$ ), a measure of the interaction probability in bulk material per unit path length traveled.

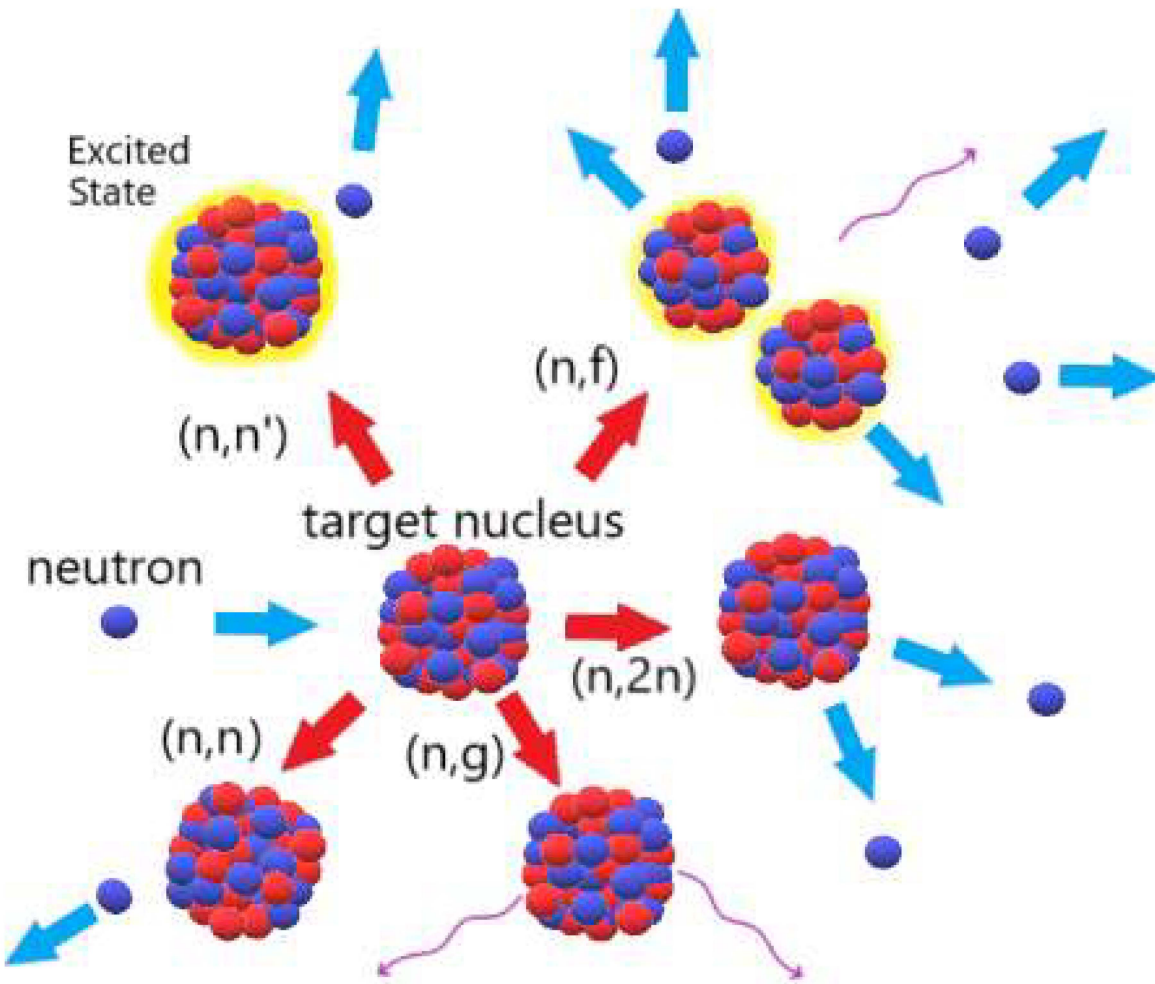


**Figure 2. Diagram of selected neutron reactions of importance to spectral shaping and fission product generation [36]**



### 2.1.1 $n,n$

Elastic scattering ( $n,n$ ) is an extremely important reaction for lowering the average energy of the neutron population by downscattering [37]. An elastic collision does not place the target nucleus in an excited state, which allows for the simplified use of conservation of energy and momentum to describe the interaction. A selected group of elastic scattering cross-sections relevant to the application in an ETA are shown in Figure 3.

The maximum energy lost in a neutron elastic collision with an isotope is a

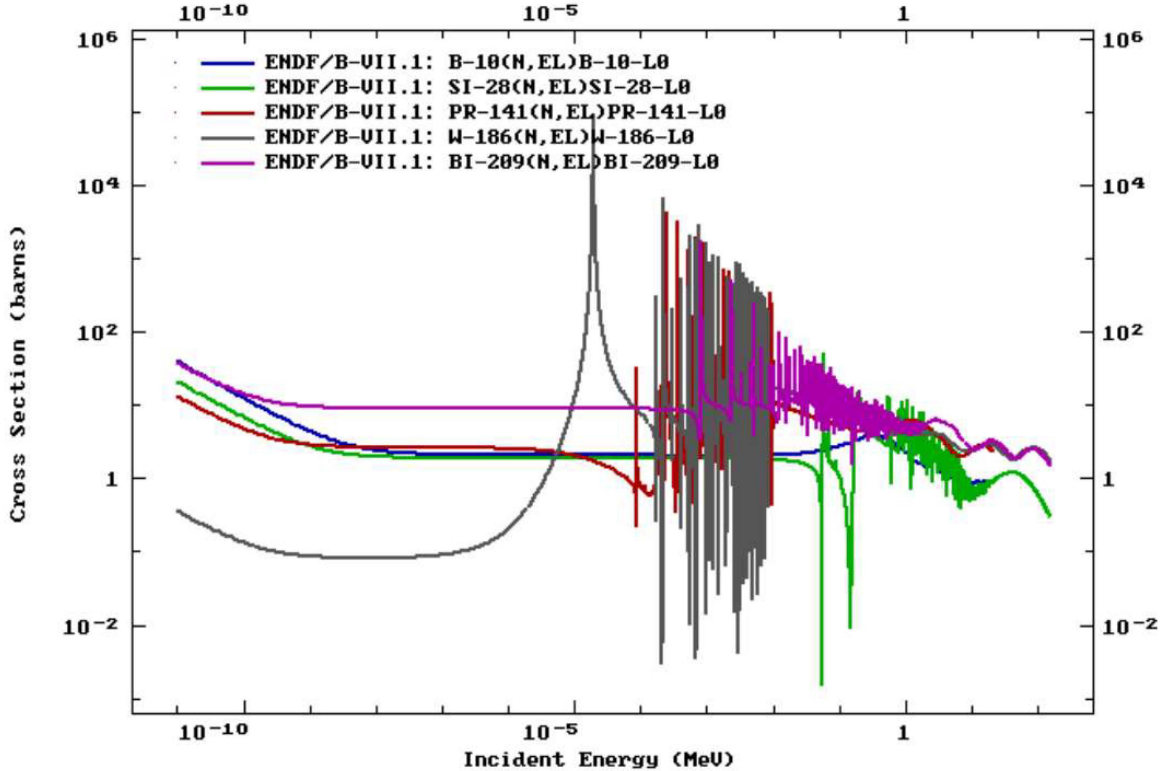


**Figure 3.** Comparison of various elastic scattering cross-sections for materials in the ETA design [1].

function of the target isotope atomic mass ( $M$ ). Elastic scattering off a higher mass isotopes produce a smaller energy loss per collision compared to interactions with low atomic mass nuclei. Elastic scattering can transfer nearly all of a neutron's kinetic energy with a collision on hydrogen, while scattering off bismuth will produce very little energy loss. The maximum energy transfer ( $Q$ ) to the target nucleus per collision is given by:

$$Q_{max} = \frac{4ME_n}{(M+1)^2}$$
[1]

### 2.1.2 n,n'

Inelastic scattering is similar to the reaction dynamics of elastic scattering; however, the target nucleus is placed in an energetically excited state [37]. These excited

states are governed by quantum mechanics and are unique to particular isotopes. An incident neutron, or other particle, can populate an excited state of the atom. For inelastic scattering, this is typically one of the lower discrete energy levels. However, the incident neutron and target nucleus can form a quasi-continuous spectrum during a compound reaction which gives rise to resonances [38].

Inelastic scattering is a threshold reaction, meaning an incident neutron must have a minimum amount of energy to enable the reaction channel. Additionally, neutrons generally lose more energy per collision on high Z isotopes if the interaction is inelastic compared to elastics. The energy that would normally be conserved in an elastic collision is reduced in the conservation equations by the energy of the state populated. Examples of inelastic scattering cross-sections are shown in Figure 4.

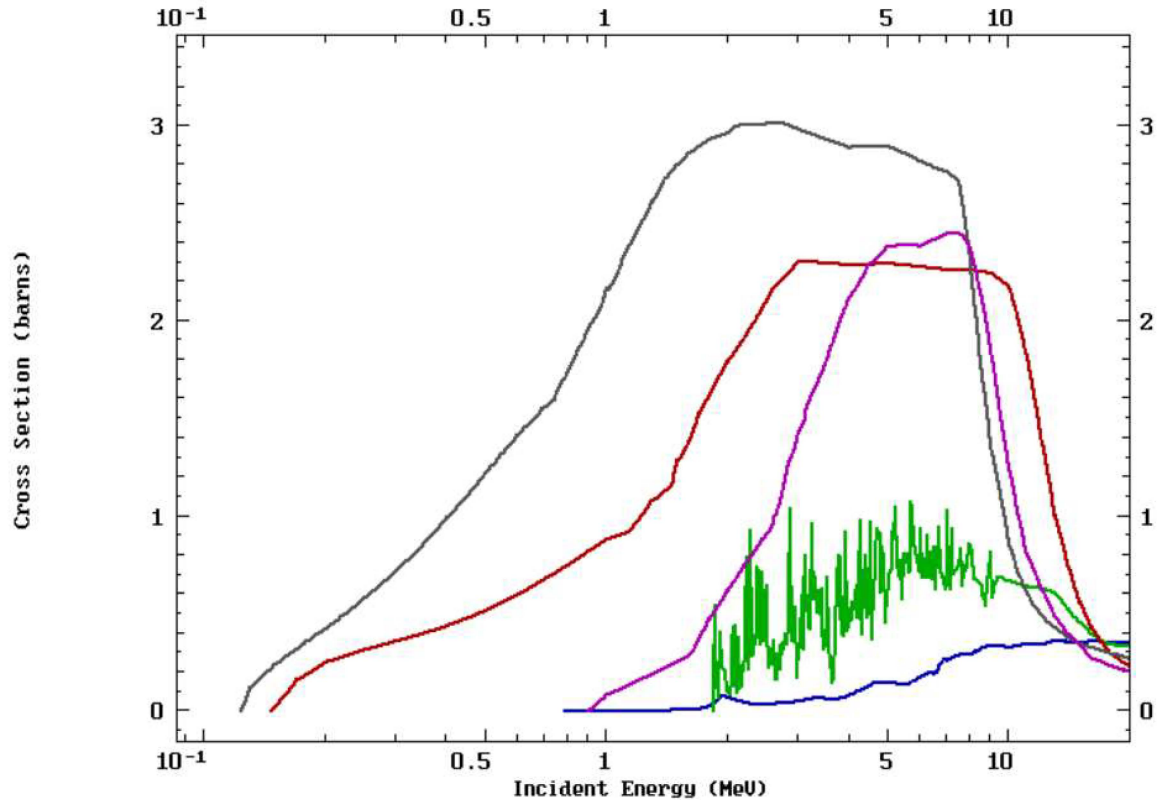


**Figure 4. Comparison of various inelastic scattering cross-sections for materials in the ETA design [1]**

Inelastic scattering is one of the lower threshold energy neutron reactions. As

shown in Figure 4, there is no general functional form of the threshold energy to enable the reaction by isotope.  $^{27}\text{Al}$ , a lighter isotope, is between  $^{184}\text{W}$  and  $^{208}\text{Pb}$ . These cross-sections indicate the energy levels of the nucleus  itself.

The excited state nucleus can de-excite via gamma emission or other channels if energetically favorable. The excited nucleus usually decays in a short time; however, metastable isomeric states can be populated with inelastic scattering and have half-lives on the order of hours or much longer [38]. These isomeric states have applications in foil activation experiments used for neutron spectrum unfolding, where it may take some time to start measuring the foil activity. An energy level and decay mode diagram of  $^{115}\text{In}$  is shown in Figure 5.

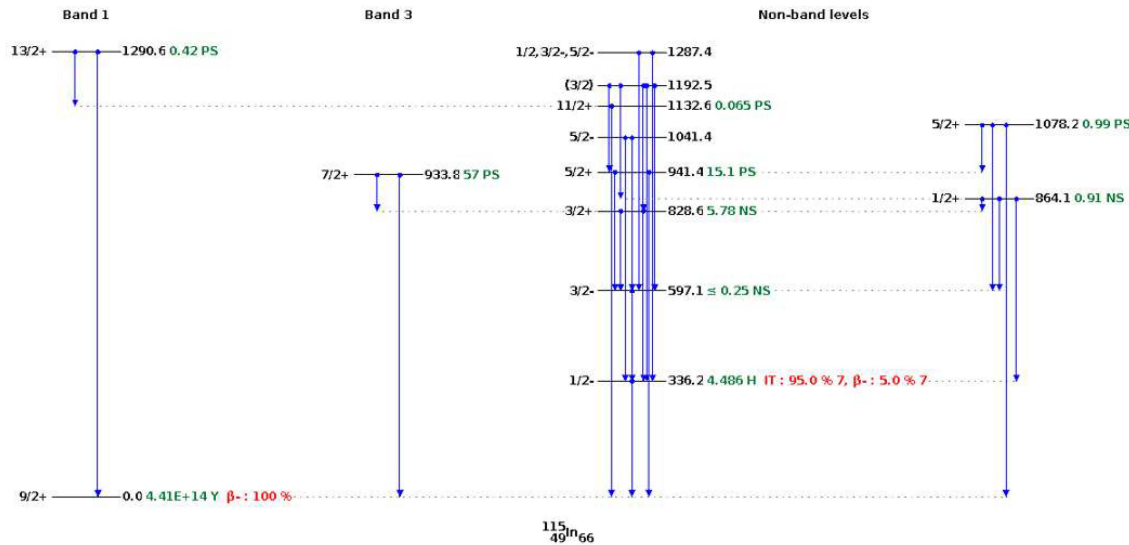


**Figure 5.**  $^{115}\text{In}$  energy level and decay mode diagram truncated at 1.3 MeV. The metastable state at 336 keV with spin parity  $J^\pi = 1/2^-$  is important for foil activation experiments for the higher epithermal region. Plots produced using the Online Service retrieval code package written by C. L. Dunford, National Nuclear Data Center, Brookhaven National Laboratory.

### 2.1.3 n,xn

A neutron can interact with a nucleus and eject additional particles, such as neutrons or protons. (n,xn) reactions such as (n,2n) and (n,3n) require a threshold

energy to separate the neutron from the original nucleus, appropriately called the neutron separation energy. Neutron separation energies are on the order of a few MeV to tens of MeV [38, 39]. Increasing the incident neutron energy allows for the evaporation of more neutrons from the nucleus.

The (n,xn) mechanism can occur as a direct reaction, where the incident neutron interacts with only a few particles in the nucleus, or as a compound reaction, where the incident neutron interact with the entire nucleus and is absorbed [37]. Example (n,2n) reactions are shown in Figure 6. The cross-section threshold is generally lower for higher atomic mass isotopes, which have neutrons that are not as tightly bound to the nucleus.

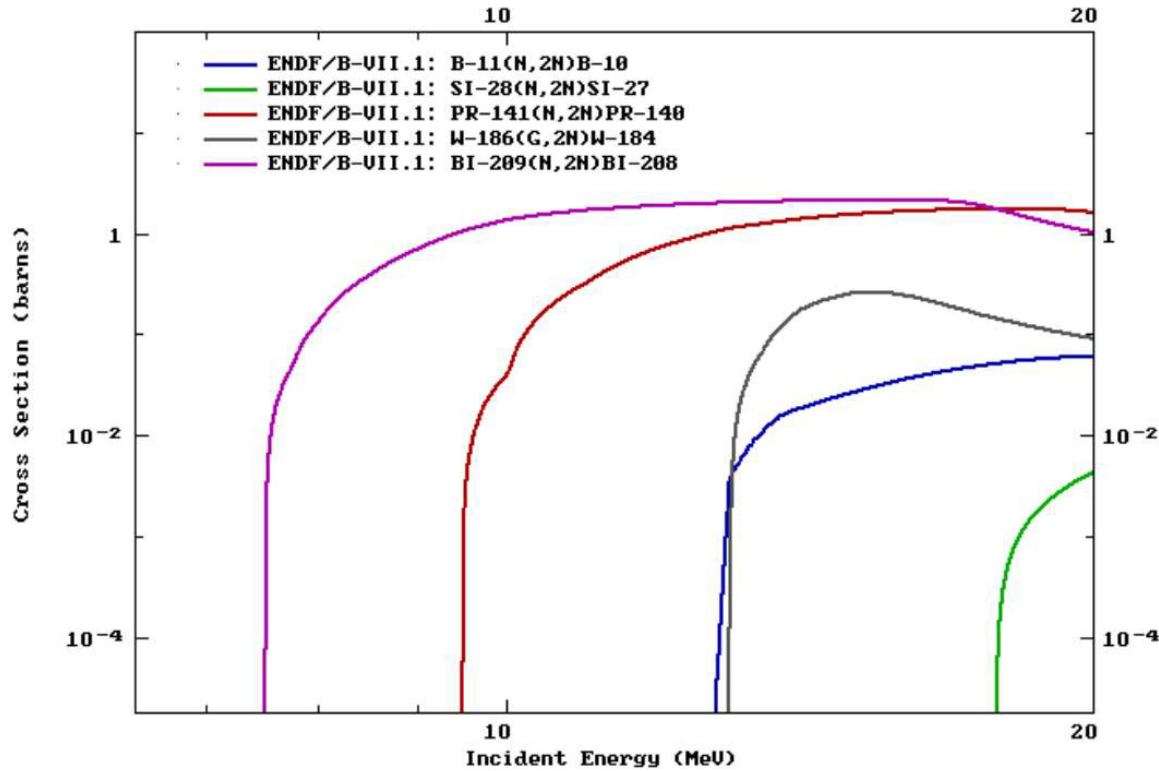


Figure 6. Comparison of various (n,2n) cross-sections for materials in the current ETA [1] 

In the context of spectral shaping, (n,xn) reactions are significant for two reasons. First, the interaction increases the total neutron population, which is beneficial for

increasing the number of neutrons on the  samples. Second, the neutron energy post-reaction is lower because the reaction required to overcome the potential barrier and losses through gamma emission. The lowered neutron energy is beneficial again for building up lower energy portions  compared to the source term. Additionally, this reaction mechanism has applications in foil activation experiments for determining the high energy neutron population.

#### 2.1.4 $n,\gamma$

Radiative capture, labeled  $(n,g)$  and  $(n,\gamma)$  in literature, is a reaction mechanism most prominent at low energies where an incident neutron is absorbed into the nucleus and a gamma-ray is emitted [38]. At low energies (below approximatley 1 keV, isotope dependent) the absorption cross-section follows the “ $1/v$ ” law, so the probability increases with the inverse of the square of  $E_n$  [37]. Figure 7 provides examples of selected  $(n,\gamma)$  cross-sections.

Radiative capture is an important absorption reaction mechanism in a few ways.  $(n,\gamma)$  reactions are of interest to foil activation experiments, specifically for determining the thermal spectrum. The resonance structure in the epithermal region can also be used to generate a unique response. Radiative capture is generally undesirable for spectral shaping, acting as a poison for the neutron economy. Fortunately, the 14 MeV NIF source, is not largely impacted by radiative capture until the neutrons have been moderated, but the  $(n, \gamma)$  reaction can be used to absorb an excess of thermal neutrons [4].

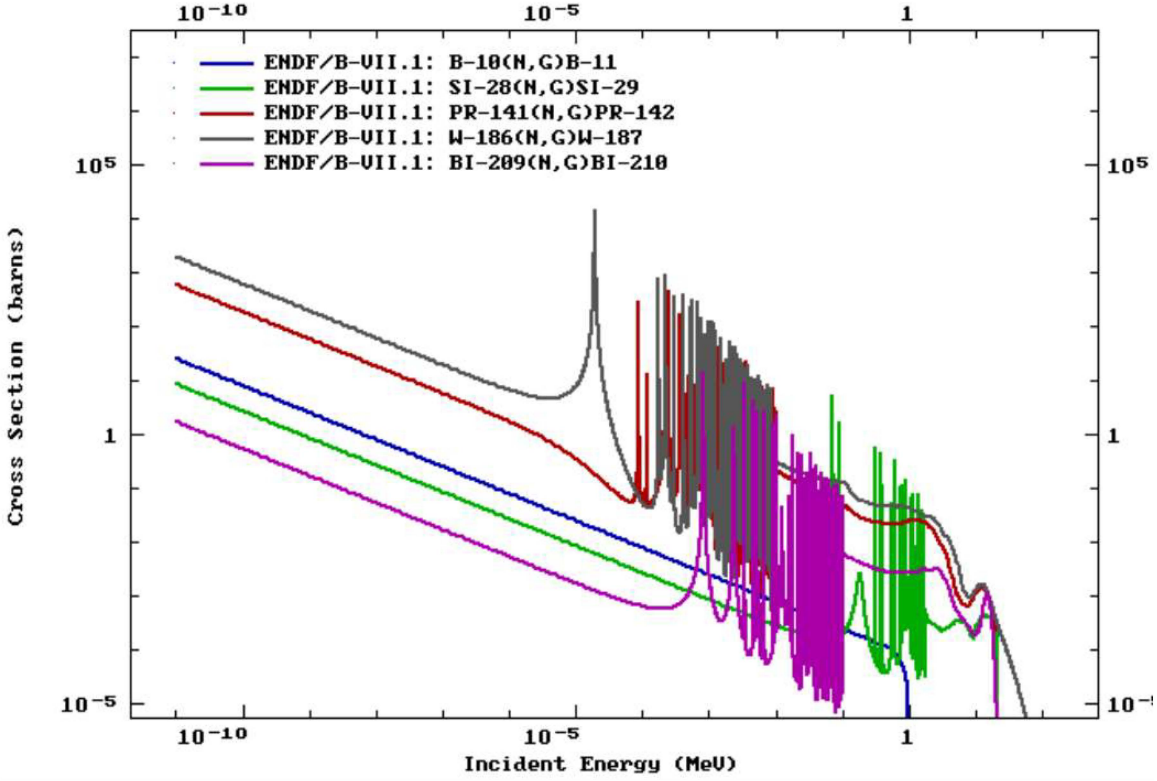


**Figure 7.** Comparison of various  $(n,\gamma)$  cross-sections [1] for materials in the current ETA

## 2.2 Nuclear Fission

### 2.2.1 Fission Theory

In nuclear fission an excited nucleus breaks up into two or more fission fragments. Fission releases a large amount of energy, which is distributed as kinetic energy in the fission fragments, neutrons, gamma-rays, and delayed decay energy. The amount of energy liberated is dependent on the specific reaction products, so an average number (approximately 200 MeV) is usually given. The delayed portion is associated with the decay of the unstable fission products, which includes energy in the form of beta ( $\beta$ ) particles, additional gamma-rays, anti-neutrinos, and neutrons. A schematic of the fission process is shown in Figure 8.

Fission occurs most often in high atomic mass nuclei, such as  $^{235}\text{U}$ ,  $^{238}\text{U}$ , or  $^{239}\text{Pu}$ ;

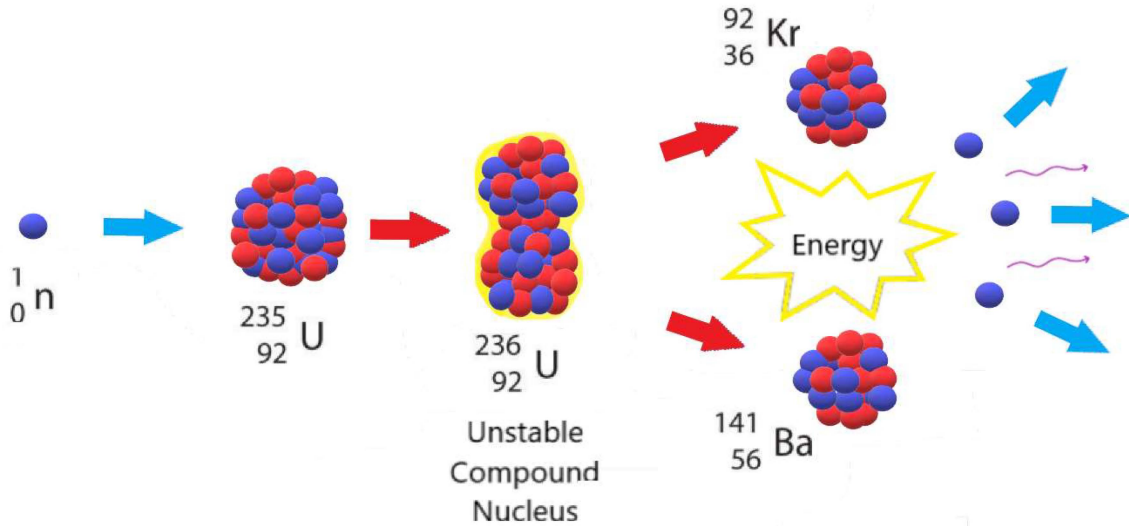


**Figure 8. Schematic overview of  $^{235}U$  neutron induced fission.**

however, any isotope can be fissioned at large enough incident energies. The fissioned isotope separates into two or occasionally three nuclei [15]. Fissionable isotopes, for example  $^{238}U$ ,  $^{240}Pu$ ,  $^{242}Pu$ , have a significant fission barrier, depressed fission cross-sections at low energy, and are incapable of sustaining a nuclear chain reaction. Fissile isotopes like  $^{235}U$  and  $^{239}Pu$  are capable of sustaining a nuclear chain reaction and have cross-sections with similar characteristics to the radiative capture cross-section shown in Figure 7.

The unstable compound nucleus can be modeled at high excitation energies, well above the fission barrier, as an incompressible liquid drop [38,40]. The deformation of the nucleus causes increased surface energies, which are balanced with the Coulomb force (charge repulsion), the strong nuclear force, and shell pairing effects. The perturbation creates an increase to the surface energy and decrease of the Coulomb repulsion because the charge is spread out [41]. During the fission process, the evolving compound nucleus can emit pre-fission neutrons, known as multi-chance fission [41]. First-chance fission is the emission of no neutrons, second-chance fission is the emission of one neutron, and so on. Multichance fission is of particular importance to

the mass chains observed in the fission product distribution.

Immediately following the fission event, the fission fragments are at a highly excited state. Fission fragments are generally very neutron rich compared to the valley of stability. The excited fragments emit photons to de-excite and may have enough energy to evaporate more neutrons [41]. The prompt fission product yield is the distribution of products post neutron evaporation from the fission fragments. The average fission process releases 2-3 neutrons, and the average increases with incident neutron energy due to multi-chance fission and an increase in fission fragment excitation energy.

### 2.2.2 Fission Products

The fission product distribution from thermally induced fission tends to be centered around isotopes with closed nuclear shells. These isotopes are have a “magic number” of protons and neutrons, similar to the filled electron structure of the noble gases. The fission fragment distribution of thermal neutrons incident on  $^{235}\text{U}$  is shown in Figure 9.

Low-Z stable nuclei have approximately equal numbers of protons and neutrons, but larger nuclei require more neutrons to mitigate Coulomb repulsion [38]. Most of the decay processes following fission are beta emitters, which occurs because the products are neutron rich and become more stable upon the conversion of a neutron to a proton. Figure 10 shows the primary decay modes of isotopes as they decay to the valley of stability. In the region of fission products, the primary competing decay mode to  $\beta^-$  is neutron emission, resulting in cross-mass chain transfers after the initial fission process.

Fission yields can be described by the independent, cumulative, and chain yields. The independent yield,  $Y_{ind}$ , is the prompt fission product distribution directly after

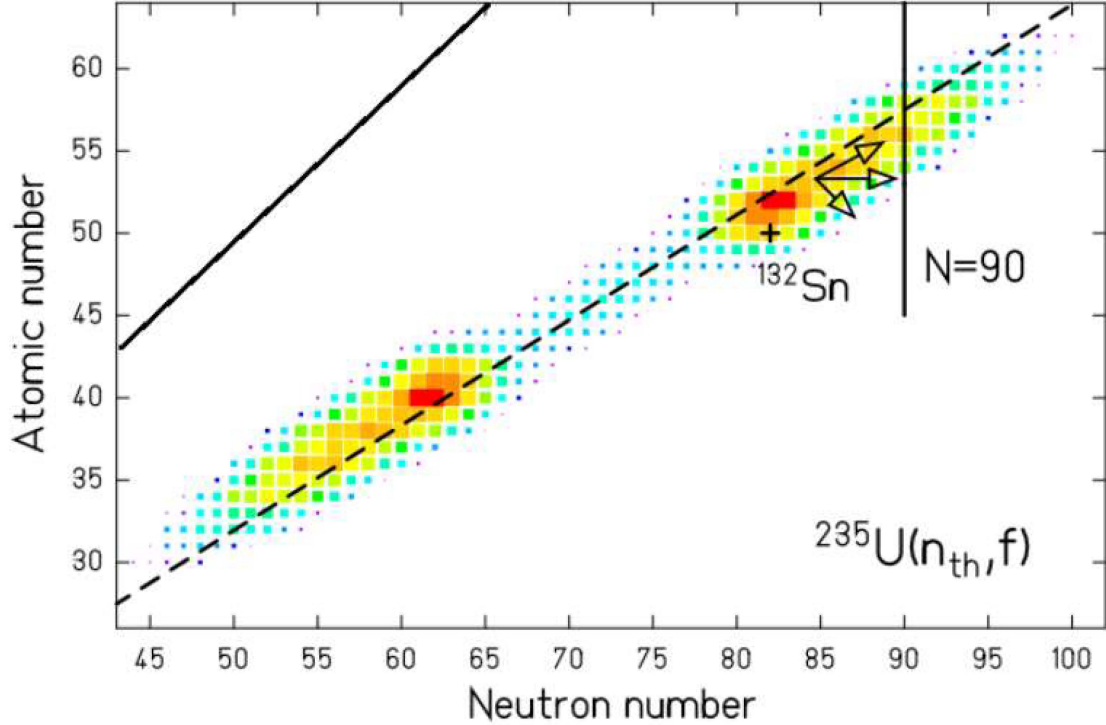


**Figure 9.** GEF calculated thermal fission product distribution prior to prompt neutron emission. The dashed line is the neutron to proton ratio of  $^{235}\text{U}$  and the solid line is a **neutron to proton** ratio of 1 [42].

the fission event before successive decay [43].  $Y_{ind}$  for  $^{235}\text{U}$  thermal fission is shown in Figure 11. The independent isomeric yield is defined as [44]

$$Y_{ind}(A, Z, I) = Y(A) \cdot f(A, Z) \cdot R(A, Z, I), \quad (2)$$

where the sum yield ( $Y(A)$ ) the sum of all independent fission products for a given mass A, the isomeric yield ratio ( $R(A, Z, I)$ ) is the production of each isomer ( $I$ ) for a given independent yield, and the the fractional independent yield ( $f(A, Z)$ ) defines the yield of a particular isotope.

The independent yield produces a cascade of decay chains leading to the cumulative yield,  $Y_c(A, Z, I)$ .  $Y_c$  represents the production of an isotope produced over all time after all prompt and delayed emissions and decays.  $Y_c$  is normally the quantity

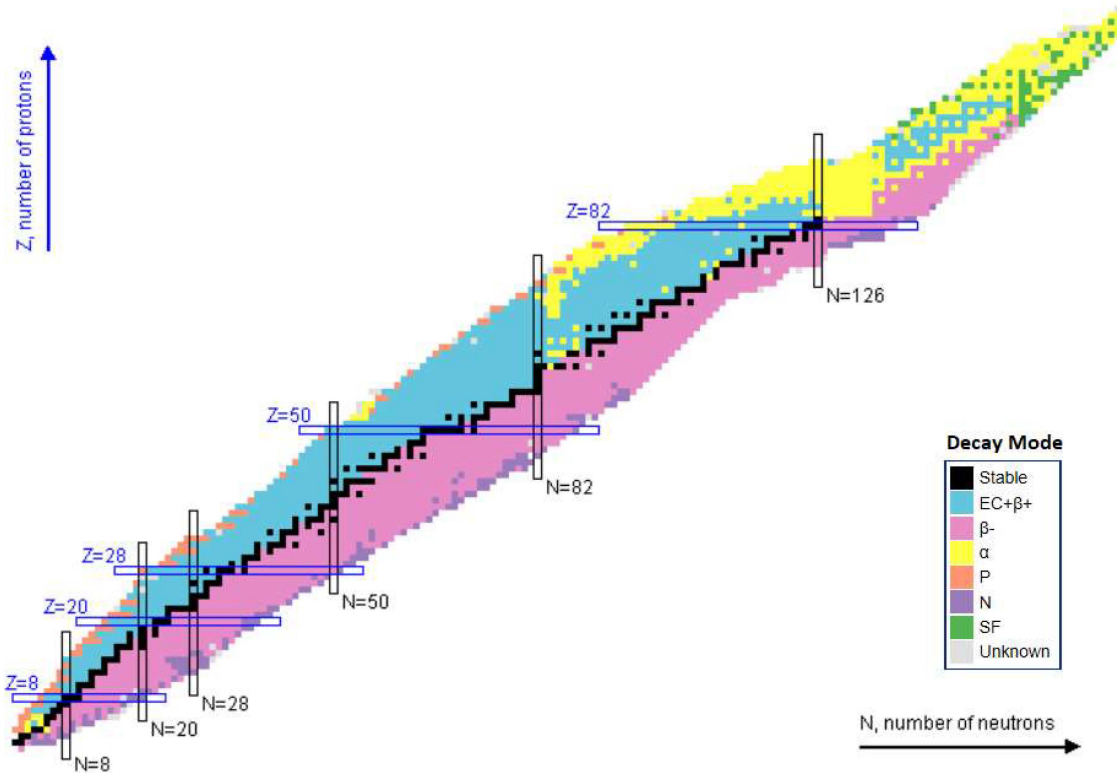


**Figure 10.** Primary decay modes of isotopes. Plots produced using the Online Service retrieval code package written by C. L. Dunford, National Nuclear Data Center, Brookhaven National Laboratory.

that is measured in experiments. The cumulative yield is given as [45]

$$Y_c(A, Z, I) = Y_{ind}(A, Z, I) + \sum_{j=0}^N Y_c(A_j, Z_j, I_j) b_j \quad (3)$$

where  $b_j$  represents the branching from isotope  $j$  into the cumulative yield and  $N$  defines the total decay channels into the cumulative yield isotope. The cumulative yields for thermal, fast, and high energy fission of  $^{235}\text{U}$  are shown in Figure 12.

As shown in Figure 12, fission product yields are dependent on the energy of the incident neutron and the fissioning nucleus. As the energy of the neutron is increased, the valley and wings of the fission product distribution are raised as the fission process becomes more symmetric [40]. The uncertainty in the fission product yields varies significantly; the fast fission relative uncertainty ranges from 1.6% for mass chain 137

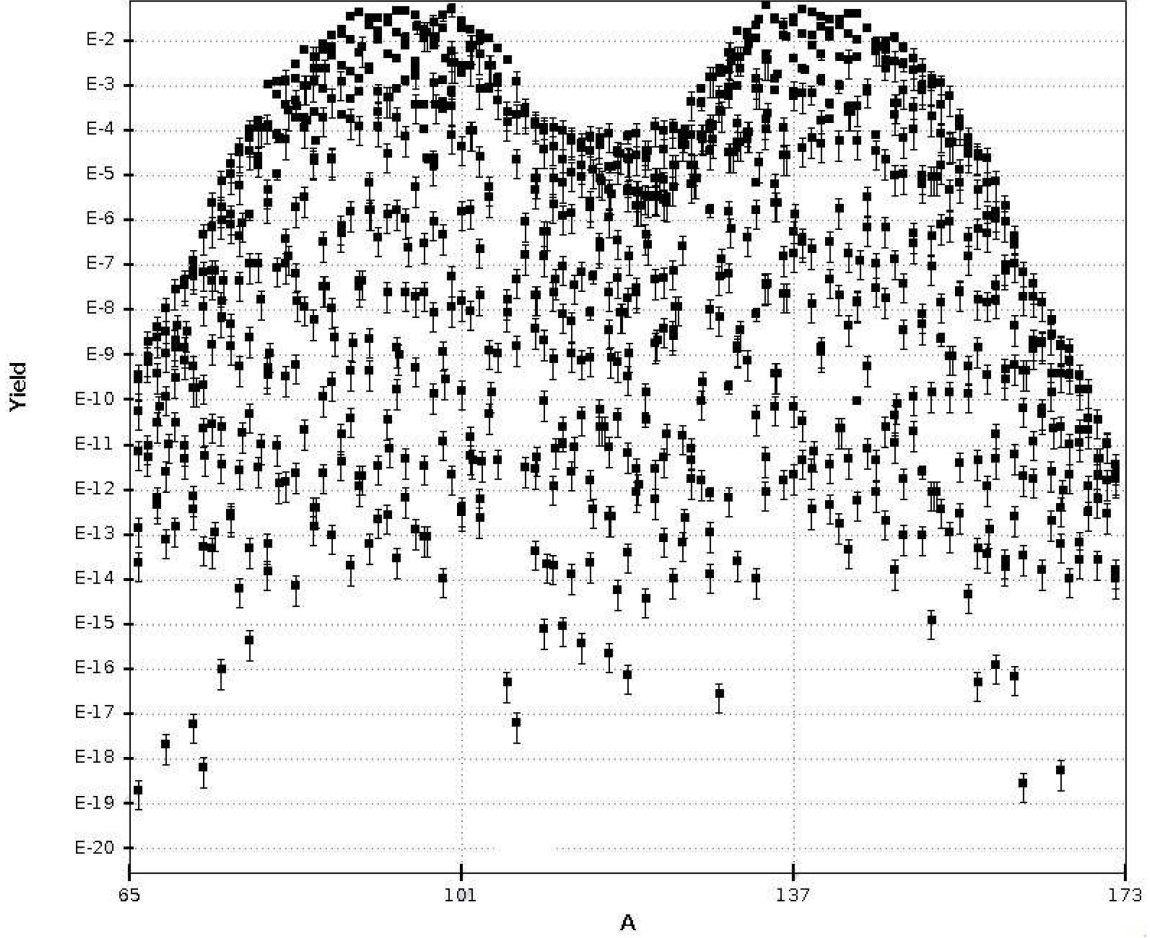


**Figure 11.** Independent fission product yield of thermal fission of  $^{235}\text{U}$ . Plots produced using the Online Service retrieval code package written by C. L. Dunford, National Nuclear Data Center, Brookhaven National Laboratory.

to 64% for mass chain 109 [1].

Finally, the chain yield for a particular mass chain is defined as the sum of the cumulative yields to the final decay to a stable or very long lived isotope in that mass chain [43]. The chain yield leads to the cumulative distribution accounting for branching in and out of a mass chain through neutron emission when; in particular, the chain yield equals the cumulative yield for the last stable member of a decay chain. An example is shown in Figure 13 for the  $A = 89$  mass chain, where the stable isotope is Y-89 [46]. The neutron deficient decay scheme has not been shown as it has negligible contribution to the fission product decay scheme.

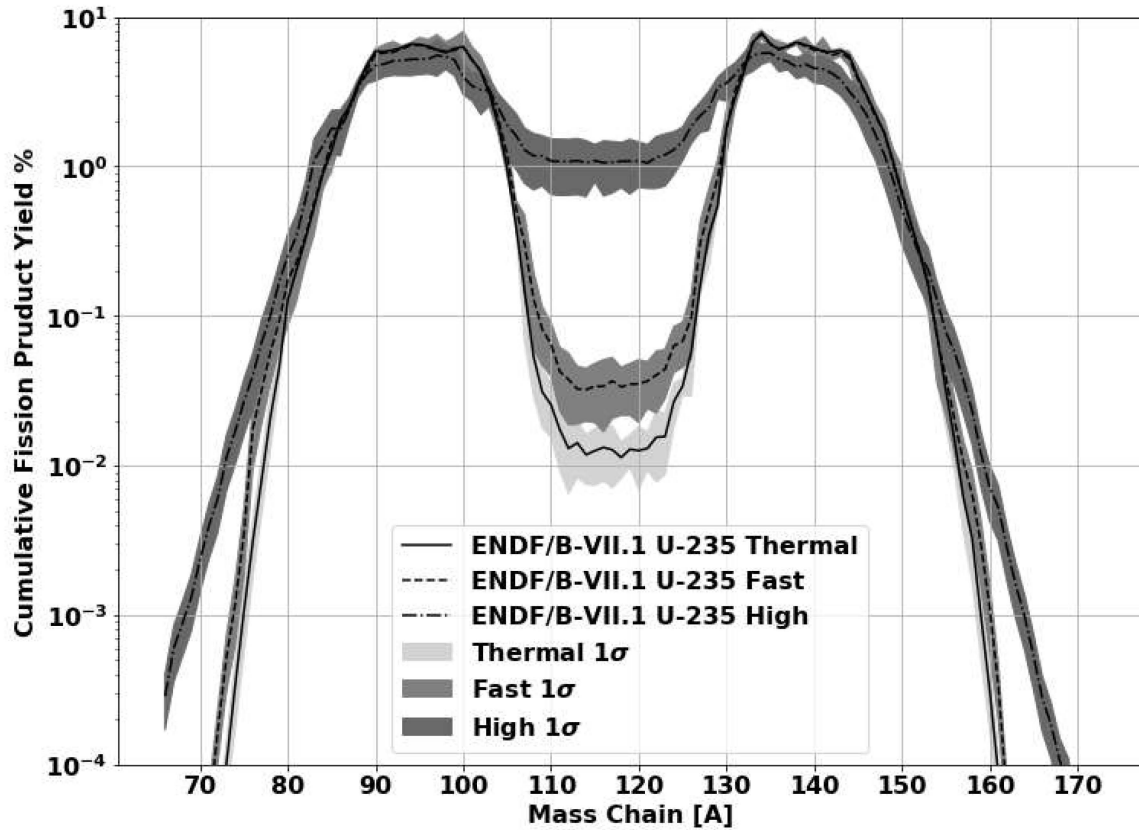


**Figure 12.** Comparison of energy dependent  $^{235}\text{U}$  cumulative fission product distributions from ENDF/B-VII.1 [1].

### 2.2.3 Nagy Fits for Fission Product Isotopes

The three fissioning isotope energies provided in ENDF describe part of the behavior of the fissioning system; however, including fit experimental data enables better energy resolution and predictions consistent with observed experiments. Empirical relations developed by Nagy provide an approach to predict the fission product yield as a function of energy given sufficient yield measurement data. Nagy fits the fission product experimental data to an exponential equation

$$Y(E_n) = Y_0 e^{bE_n} \quad (4)$$

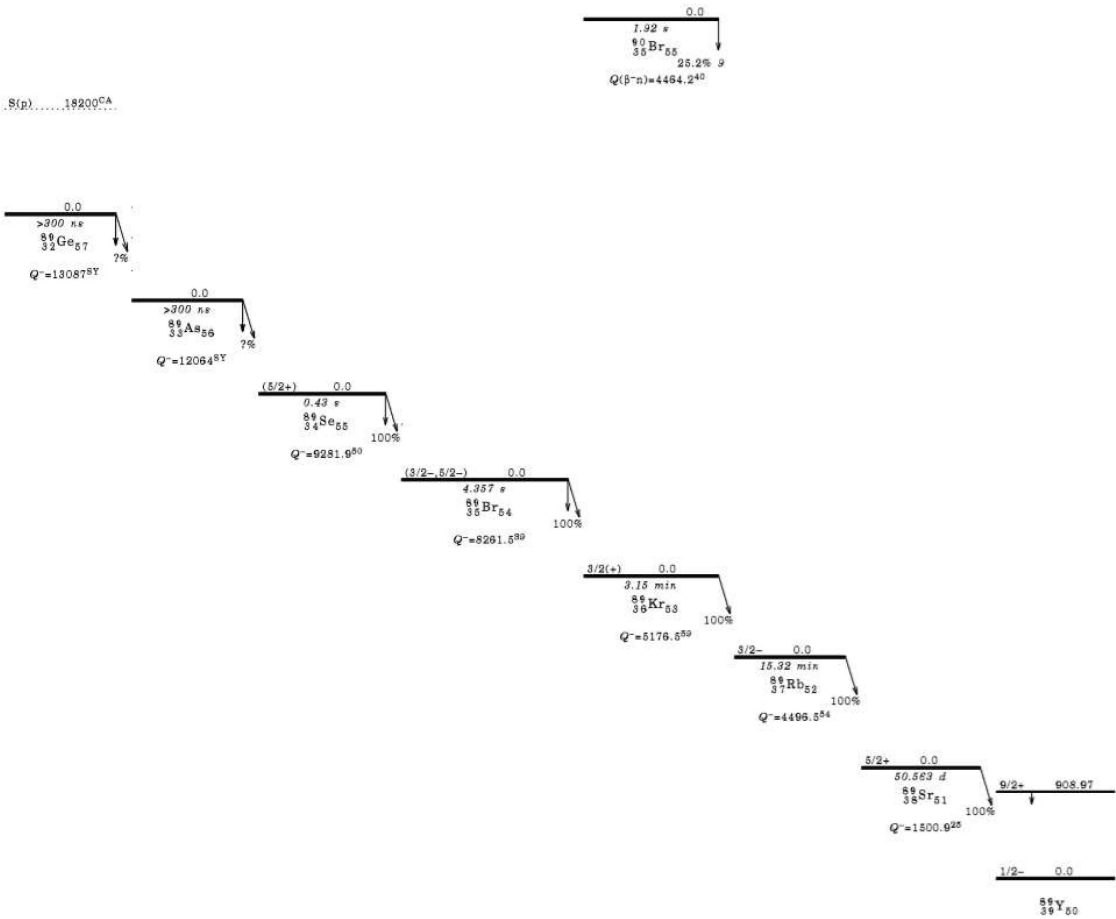


**Figure 13.** Neutron rich decay scheme for mass chain A=89 where the  $^{89}\text{Sr}$  decay to  $^{89}\text{Y}$  represents the final decay to the stable isotope [46].

where the fitting parameters  $b$  and  $Y_0$  represent the slope of the function in logarithmic form and thermal fission yield, respectively [34]. The slope is the primary measure of the energy dependency of the fission product yield, which requires modifications for multi-chance fission. First chance fission is dominant from up to 5.5 MeV, and second-chance fission up to 14.1 MeV [34]. Multi-chance fission effects on the fission product yield are less pronounced in asymmetric regions but can have a large impact in symmetric fission ( $109 \leq A \leq 129$ ) [4] [34].

It is important to note that data based phenomenological models are not perfect predictors of determining fission products **a priori**. In particular, recent pub-

lications have findings that cannot be accurately modeled with current theoretical approaches [40]. In general, there are large uncertainties in the predictive power of calculating energy dependent fission product yields. Still, this type of empirical fit is more predictive than GEF for individual isotopes where sufficient energy dependent measurements exist.

## 2.3 Nuclear Data

### 2.3.1 Nuclear Data Libraries

Nuclear data relevant to neutrons has been collected for the better part of the last century. Nuclear data available for modeling and simulations is collected and published in evaluated data files. There are many versions of evaluated nuclear data, which all aim to characterize the relevant physics backed by experimental results. For example, the primary U.S. based nuclear data file is the Evaluated Nuclear Data File (ENDF). Other nations or organizations also have independent evaluations of the available nuclear data. Examples of other nuclear data libraries are the Russian National Library of Nuclear Data (ROSFOND), the European Joint Evaluated Fission and Fusion (JEFF) Nuclear Data Library, and the International Reactor Dosimetry and Fusion File (IRDFF).

Figure 14 shows the evaluation of  $^{197}\text{Au}$  ( $n,2n$ ) reaction for various libraries. In some cases, the library evaluation can be drastically different. However, sometimes the libraries are drawing from the same data and models, which can be noted by the overlapping evaluations.

The experimental data that feeds into ENDF is contained in EXchange FORmat (EXFOR), where the experiment uncertainty, if available, is tracked. Experiments with sub-electron-volt neutron energy resolution are not feasible at the present time, so the nuclear data evaluators need reaction models to fill in the gaps. ENDF relies on

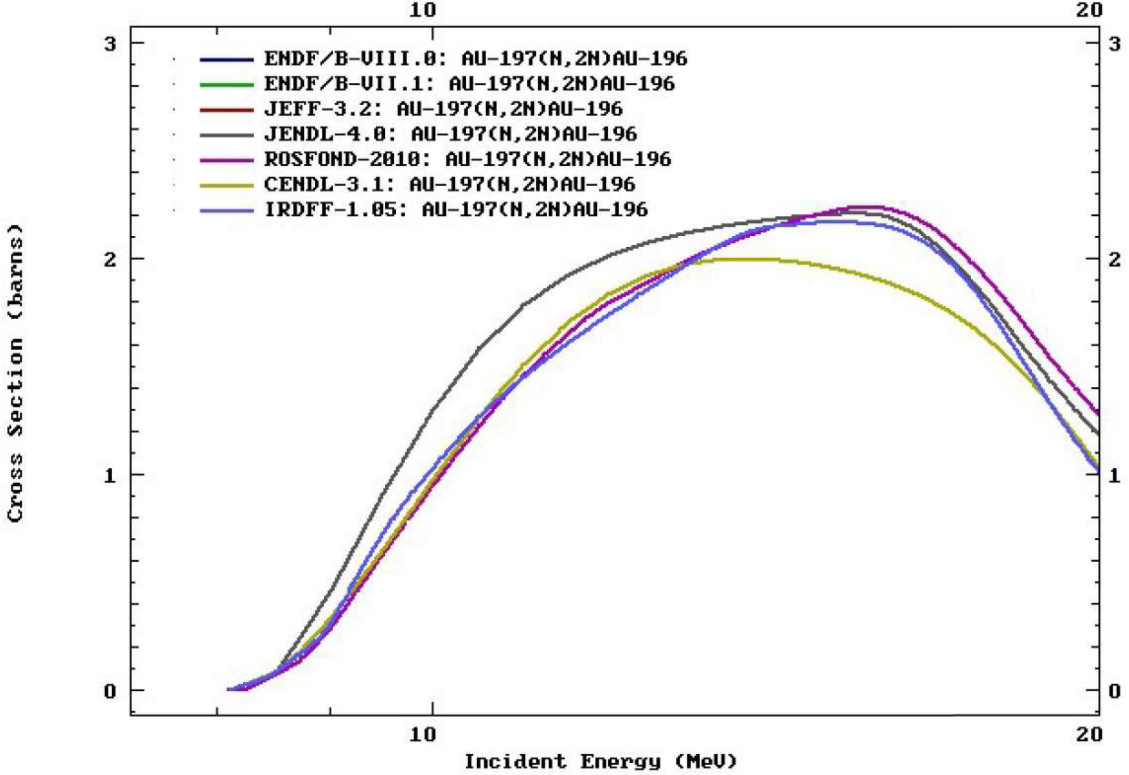


**Figure 14.** Comparison of various library evaluations of the  $^{197}\text{Au}$  ( $n,2n$ ) cross-section [1].

evaluations of EXFOR data based on experimental quality, statistics, and theoretical basis to fill in areas lacking experimental data [47]. ENDF then stores the underlying nuclear data (cross-sections, angular distributions, half-lives, ect.) that can be used in simulations.

Benchmarking the evaluated nuclear data is done primarily through testing of integral results, such as the effective neutron gain to loss ratio ( $k_{eff}$ ) of a critical assembly [47]. These integral measurements provide a more accessible measurement that can be done with high precision and accuracy, as precise as a relative error of 0.01%, to validate microscopic cross-sections. The use of integral benchmark experiments is important for comparing the net result of the nuclear data; however, there are uncertainties and correlations in the independent reactions that combine to create the integral results.

Each library is **iterated on** with validation experiments, applications, studies, and integral benchmarks to increase the base and accuracy of the nuclear data [47]. However, It is important to note that the experiments used to measure nuclear data may have uncertainty that varies by orders of magnitude. An interesting feature of this fact is that the relative nuclear data uncertainty does not always decrease over time that the reaction is studied. One example is the increase in uncertainty in the neutrons released per thermal fission of  $^{235}\text{U}$ , which increased from 0.311% to 0.385% between ENDF/B-VII.0 to VII.1 [48]. Another example demonstrating the nuclear data problem is that  $^6\text{He}$  half-life has changed by approximately 5% with large increases in the relative error over the last 50 years [49].

Another prevalent issue is that the majority of accurate measurements were performed for nuclear reactor studies, which limits accessibility to reliable data for different applications. As a consequence of this, ENDF only contains fission production data at thermal, fast (0.5 MeV), and high energy (14 MeV). To combat this challenge, smaller, more application specific libraries have been developed.

The International Atomic Energy Agency **provides** (IAEA) provides data for the benchmarked neutron dosimetry reaction IRDFF library [50]. This library is noted because it is used in the PNNL STAYSL code system, discussed in Section ???. The IRDFF v.1.05 library contains “state-of-the-art” covariance information and has continuous improvement through testing and integral experiments [51].

The IRDFF library also includes feed through from fast decaying excited states to metastable states for important dosimetry reactions. An example is the  $^{115}\text{In}$  ( $n,n'$ )  $^{115m1}\text{In}$  reaction; the  $^{115m1}\text{In}$  reaction product decay scheme was depicted in Figure 5. The first metastable state at 336 keV (spin parity  $J^\pi = 1/2^-$ ) has a half-life of 4.5 hours, which makes it a good candidate reaction for foil activation experiments [52]. The IRDFF v.1.05 library contains reaction data that includes the

decay of additional metastable states and higher excites states into  $^{115m}1\text{In}$ . Under standard measurement timing conditions, all of the higher energy  $^{115}\text{In}$  states will have decayed, thus contributing to the activity measured for the first metastable state.

### 2.3.2 Nuclear Data Covariance

Covariance arises in nuclear related experiments when one process impacts another or the nuclear data measurement energy ranges are correlated. Unfortunately, nuclear data covariance analysis is not standard to experimental analysis. Often errors are attributed to model fidelity, measurement, or setup problems when nuclear data covariance may have been the root cause [53]. In many nuclear decay processes, the correlation between decays is unity because the decays happen in a series. However, covariance can occur if there is branching from a radioactive state. Covariance is defined with the expectation values,  $\langle X \rangle$ , and mean value ( $\mu$ ) providing for the covariance between variables X and Y as

$$cov(X, Y) = \langle XY \rangle - \mu_X \mu_Y, \quad (5)$$

A correlation matrix combined with the uncertainty in the nuclear data can be used to form the covariance matrix. The diagonal of the correlation matrix is one, so the diagonal of the covariance matrix is the variance for the group. As such, the covariance of an observable compared to itself reduces to the variance

$$cov(X, X) = \langle X^2 \rangle - \langle X \rangle^2 = \sigma_X^2. \quad (6)$$

The conversion from a correlation matrix to a covariance matrix is given by

$$\text{cov}(X, Y) = \text{corr}(X, Y)\sigma_X\sigma_Y. \quad (7)$$

Instead of the covariance matrix, nuclear data often stores the correlation matrix in a group structure format, as shown in Figure 15. In general the largest correlations occur in nearby energy groups, where the experimental uncertainty in the incident  $E_n$  is largest. Correlations also exist between reactions, in addition to correlations in a single energy dependent reaction channel, but this data is rarely quantified.

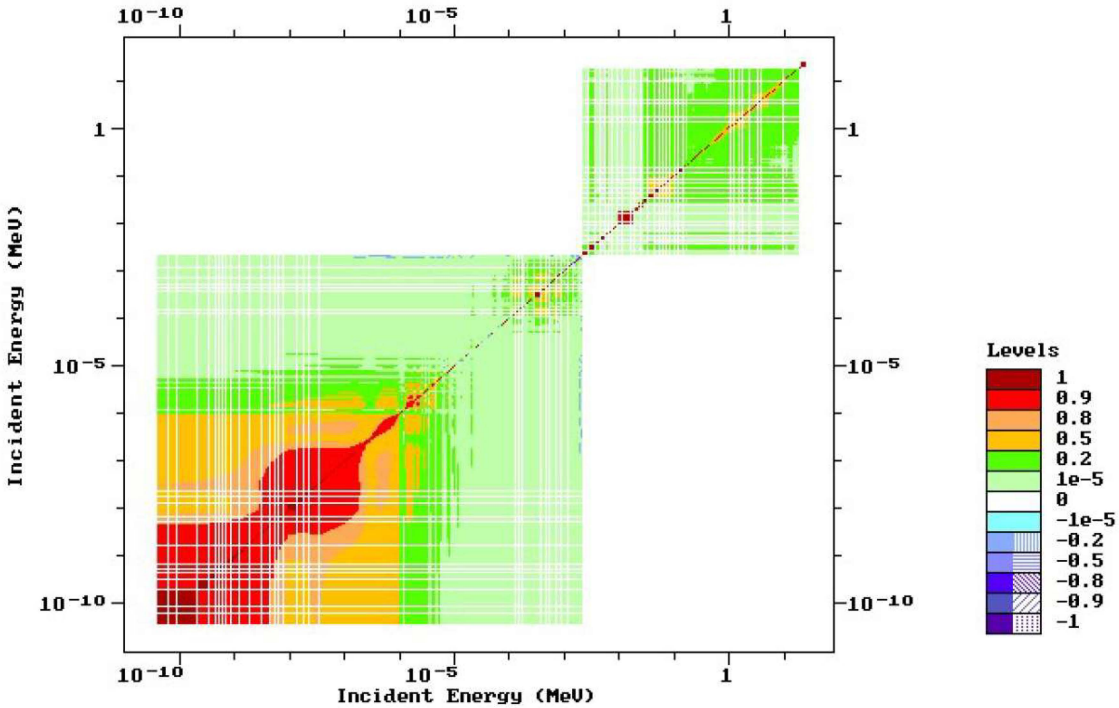


**Figure 15.**  $^{235}\text{U}$  (n,f) correlation matrix [1].

Integral experiments are extremely dependent on the underlying reactions that make up the net result. Therefore, there are generally larger variances in the the reactions that are part of the total cross-section. Figure 16 displays the relative uncertainty of the  $^{235}\text{U}$  (n,f) cross-section compared to the total. Figure 17 displays the total cross-section of  $^{209}\text{Bi}$  compared to the (n,2n) reaction.

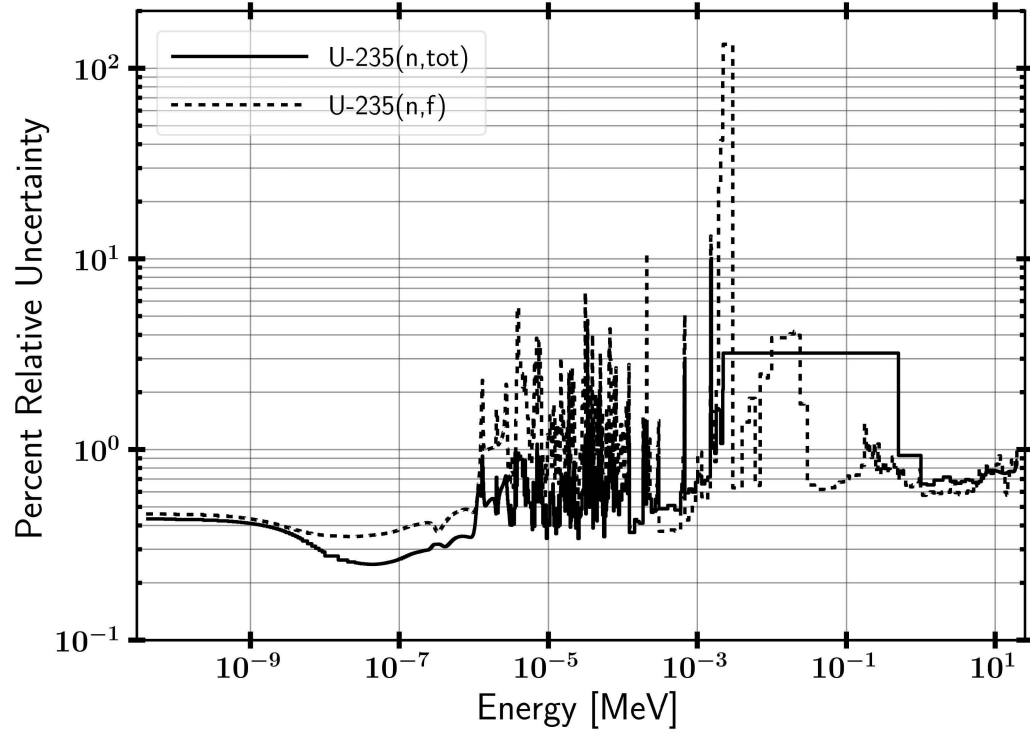


**Figure 16.**  $^{235}\text{U}$  (n,f) compared to  $^{235}\text{U}$  (n,tot) cross-section uncertainties [1].

The uncertainty in  $^{235}\text{U}$  (n,f) and  $^{209}\text{Bi}$  highlight a couple key attributes relevant to nuclear data. First, the component reactions that make up the integral cross-section almost always have a higher relative uncertainty because integral, total cross-section experiments can more accurately be measured through attenuation of a “beam” of neutrons. The underlying reactions are generally more difficult to characterize. Second, the  $^{235}\text{U}$  (n,f) relative uncertainty near 2.2 keV is 133.6%, which implies that when utilizing a Gaussian distribution the cross-section must go negative to capture the full distribution of possible total cross-sections within a given confidence interval. This is obviously non-physical; however, it gives scope to the magnitude of uncertainty of the underlying cross-sections over difficult experimental energy ranges. Next, the  $^{235}\text{U}$  reactions are more thoroughly studied as compared to  $^{209}\text{Bi}$ . Over the majority of the energy range,  $^{235}\text{U}$  is below one percent relative error, largely driven down by thermal nuclear reactor experiments, while  $^{209}\text{Bi}$  has a

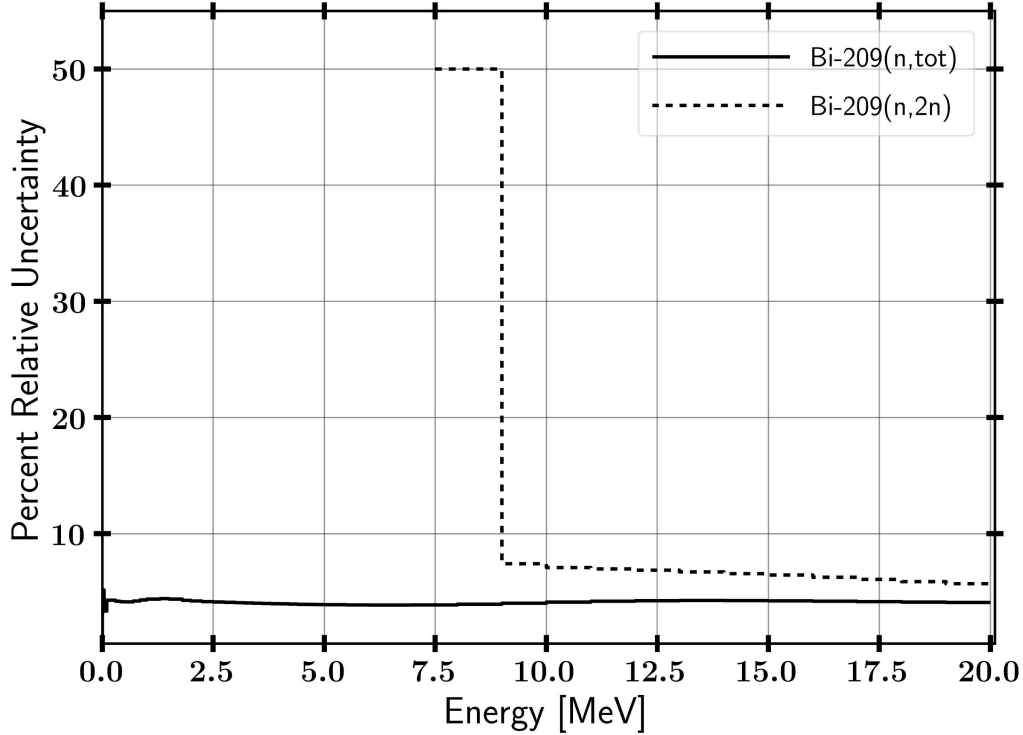


Figure 17.  $^{209}\text{Bi}$  (n,2n) compared to  $^{209}\text{Bi}$  (n,tot) cross-section uncertainties [1].

larger error around five percent. Finally, areas where the cross-sections are low have representative larger relative errors; this is the case near the threshold of the  $^{209}\text{Bi}$  (n,2n) reaction shown in Figure 17.

### 2.3.3 Nuclear Data Stochastic Sampling

The two primary methods that exist for uncertainty quantification of radiation transport simulations are linear perturbation and stochastic sampling Monte Carlo approaches [54]. First order linear perturbation theory is not always adequate for large uncertainties or incorporating second order effects from the uncertainty in the neutron transport; however, it does have broad uses in the reactor community. Stochastic sampling has grown in popularity as computational resources have improved. Stochastic methods rely on performing independent neutron transport calculations with perturbed nuclear data libraries sampled based on the covariance of the cross-sections

using the multivariate normal distribution to build up a distribution of responses [55]. The generalized multivariate normal distribution as a function of the nuclear cross-section mean values ( $\mu$ ) of length k, random solution vector ( $\mathbf{X}$ ), covariance matrix ( $\Lambda$ ) is given by

$$f(\mathbf{X}) = \frac{\exp(-0.5(\mathbf{X} - \mu)^T \Lambda^{-1} (\mathbf{X} - \mu))}{\sqrt{(2\pi)^k |\Lambda|}}. \quad (8)$$

Several Monte Carlo sampling methods have been created to capture the impact of nuclear data covariance on nuclear engineering problems, including SCALE Sampler, NUSS, SHARK-X, amongst others [56] [57] [58] [55]. Many collections of software capable of performing these types of uncertainty quantification are not available for distribution or focus solely on reactors.

Deficiencies with the stochastic sampling approach are generally associated with the nuclear data libraries utilized and the sampling method. First, nuclear data uncertainty is often above 100% in energy regions where a measurement was never taken, so the value of the cross-section is not well characterized. Second, the nuclear data uncertainty is assumed to be normally distributed; however, alternative forms may be more appropriate. In stochastic sampling approaches, these two factors leads to truncation of large uncertainties to prevent performing neutron transport calculations with negative cross-sections. Although negative cross-sections are non-physical, the truncation may underestimate the uncertainty which can have an impact if the experiment is performed in these energy domains when using the Gaussian distribution. Finally, component cross-sections which make up the total cross-section are constrained to add up to the total cross-section.

## 2.4 Monte Carlo Neutron Transport

### 2.4.1 Monte Carlo Neutron Transport Theory

Monte Carlo methods for neutron transport leverage pseudo-random sampling,<sup>1</sup> the nuclear data,<sup>2</sup> and material specifications to build up a simulation of the particle transport in space, direction, energy, and time [59]. Neutron interactions are sampled with probability distribution functions (PDFs) for aspects such as path length traveled and interaction type [60].

An objective of a neutron transport calculation is to determine the average behavior of particles within the system. This can be captured with the volume averaged scalar flux,  $\bar{\phi}_V$ , defined as

$$\bar{\phi}_V = \frac{1}{V} \int_V dV \int_t dt \int_E dE \phi(\vec{r}, E, t), \quad (9)$$

where  $\bar{\phi}_V$  is given as a function of energy ( $E$ ), position ( $\vec{r}$ ) and time ( $t$ ). Monte Carlo methods approximate the scalar flux with either track length or collision estimates [60]. The track length estimator is

$$\bar{\phi}_V = \frac{W T_l}{V N}, \quad (10)$$

where the path length score for the flux is based on the length traveled ( $T_l$ ) and is normalized by the particle weight ( $W$ ), cell volume ( $V$ ), and number of histories sampled ( $N$ ).

Statistics often drive the uncertainty in a Monte Carlo simulation as systematic uncertainties are generally not considered due to computational costs. The “true” mean value,  $\mu$ , of a response PDF is the expectation value,  $E(x)$ , which is estimated with a sample mean,  $\bar{x}$ . According to the Central Limit Theorem, the sample mean approaches the real mean as the number of samples,  $N$ , goes to infinity, and the

distribution of sampled  $x_i$  follows a Normal distribution. The sample mean can be calculated as

$$\bar{x} = \frac{1}{N} \sum_{i=1}^N x_i. \quad (11)$$

Therefore, sample variance, ( $S_x^2$ ) can be computed as

$$S_x^2 = \frac{1}{N-1} \sum_{i=1}^N (x_i - \bar{x})^2, \quad (12)$$

and the variance of the mean, ( $S_{\bar{x}}^2$ ), is simply

$$S_{\bar{x}}^2 = \frac{S_x^2}{N}. \quad (13)$$

where  $S_x^2$  is defined as Therefore, the statistical uncertainty in the results decreases with  $\sqrt{N}$ . The precision of the result can be improved with more histories, shrinking the spread in  $x_i$ . However, the accuracy cannot be improved. Accuracy is impacted by systematic errors, such as uncertainty in the nuclear data.

#### 2.4.2 Comparison of Monte Carlo Neutron Transport Results

The results from different Monte Carlo simulation codes often produce slightly different results. The outputs are generally in better agreement for criticality calculations of critical assemblies and nuclear reactor analysis. It is important to gauge the impact of utilizing different transport codes to see how much variance is expected. Some of the differences that impact Monte Carlo simulations are within the structure of the code itself, statistical error, or different starting seeds, while others are based on the nuclear data that may be altered, geometry or source implementation, or user error.

Criticality is a well-understood nuclear engineering problem that the nuclear data

libraries are validated against. A study conducted on a high temperature pebble-bed reactor compared SCALE’s CSAS6 module for criticality calculations to MCNP5’s kcode [61]. The results showed a difference for calculating  $k_{eff}$  to be on the order of a few hundred percent  $\text{mile} (10^5 * (k_{eff} - 1)/k_{eff})$ . This variance can easily be handled for reactor operations; however, this highlights that even well understood problems do have differences based on operating code. A similar study of a pebble bed reactor determined that the difference in  $k_{eff}$  in MCNP to SCALE was near half a percent [62]. Another study compared the average gamma-ray dose outside of a spent nuclear fuel cask [63]. The difference in dose rates between the modeled SCALE and MCNP simulations varied as much as 27%. Again, this shows that the less benchmarked studies can have large code-to-code disagreements.

## 2.5 Foil Activation

### 2.5.1 Foil Activation Theory

Foil activation is a method of characterizing an incident neutron flux through unfolding the response of the foils using the energy dependent nuclear reaction channels in the foil. Activation experiments are essential for testing that requires small geometry to fit in the apparatus or where electronics equipment for higher fidelity measuring techniques will be damaged.

Activation foils produce measurable radioactive isotopes during the course of irradiation. The production rate of radioactive isotopes is negated by radioactive decay processes, which place an upper limit on the radioactivity of a foil [64]. The saturated activity

$$A_\infty = R = \int_{E1}^{E2} \phi(E) \Sigma(E)_{act} V. \quad (14)$$

is equivalent to the reaction rate ( $R$ ), which is a function of the energy dependent flux ( $\phi$ ), the macroscopic reaction activation cross-section ( $\Sigma(E)_{rxn}$ ), and the volume of the foil ( $V$ ). The energy term ( $E1$ ) is zero in many cases; however, threshold reactions require the incident neutron to be of higher energy to enable the reaction channel.

At six half-lives, a foil will have reached approximately 98% of its saturation activity, neglecting spatial and energy self-shielding effects [64]. When the activation is not sufficient to fully saturate the foil, a correction needs to be made. The activation of the foil for a given irradiation time ( $t_i$ ) is given as

$$A_0 = A_\infty(1 - e^{-\lambda t_i}). \quad (15)$$

where  $\lambda$  is of the decay constant of the radioactive product.

The formula can be simplified in the limit of irradiation times much less than the half-life of the activation products. In this case, the reaction rate is much larger than the decay from radiation, so the rate of production of the radioisotope is driven only by the reaction rate. The neutron pulse length at the NIF is on the order of shakes, so this approximation can be made for the foil activation. The time integrated flux, or neutron fluence ( $\Phi$ ), can be used to determine the total reactions, ( $R_{total}$ ), over an irradiation period, given by:

$$R_{total} = \int_{E1}^{E2} \Phi(E) \Sigma(E)_{act} V dE \quad (16)$$

Experimental measurements of the activity must be corrected to deduce the original activity of the foil ( $A_0$ ) immediately after irradiation as shown in Equation 17. The activity is corrected for the radioactive decay for the time between the end of irradiation and the start of counting ( $t_d$ ). A similar correction factor based on the count

time ( $t_c$ ) provides a correction for radioactive decay during counting that can result in a reduction of counting rates by the end of the counting period. Additionally, the detector efficiency for the given gamma-ray energy ( $\epsilon$ ) and relative gamma intensity ( $I_\gamma$ ) must be taken into account. The gamma intensity may also include a branching ratio if applicable to the decay mechanism. Finally, the measured counts ( $C$ ) is reduced by the background counts ( $B$ ). All corrections included, less self-shielding effects, provide a formulation for converting counts to post-irradiation activity as:

$$A_0 = \frac{\lambda(C - B)e^{\lambda t_d}}{\epsilon(1 - e^{-\lambda t_c})I_\gamma} \quad (17)$$

### 2.5.2 Selection of Experimental Foils

The method of foil activation has been studied in-depth in the nuclear sciences and engineering community. A list of the various requirements that are of importance for a neutron activation foil experiment with energies in the range of thermal to approximately 20 MeV are summarized below [59, 64, 65].

- The reaction neutron cross-section is extremely important for foil activation, and there are a few key parameters that should be considered. First, the magnitude of the cross-section determines the reaction rate of the product nuclides. A large cross-section allows for more activation, and therefore, better results when analyzing the activation foils. Second, the uniqueness of the cross-section shape is used to unfold the incident neutron energy spectrum. An  $(n,\gamma)$  cross-section may peak in a particular region, which is essential to providing information of the neutron flux in that energy region. Alternatively, a threshold reaction, such as an  $(n,2n)$ , is important for providing information of the flux at higher energies. Third, the selected foils for an experiment should cover the entire energy range of the incident neutron flux. Finally, the cross-section must be well

characterized with low uncertainty over the neutron energy range of interest.

- The range of activation product half-lives applicable for a particular experiment depend on availability of detectors and the foils post-irradiation. A long lived radioisotope will be available for counting for longer times at the expense of the total activity. The opposite is true for short half-lives. Half-life<sub>ee</sub> on the order of an hour to a few years are generally used; however, the half-life must also be balanced with the production of the radioisotope to understand the entire picture.
- The elemental and chemical purity of the activation foil should be well known. An unknown composition foil can produce erroneous results.
- Interfering reaction channels and decay emissions should be avoided. An example of this is natural copper, which has multiple 511 keV emissions from different reaction channels. It is difficult to distinguish these gamma-rays to determine activation in counting. Similar problems arise in multi-isotope materials that have multiple reactions producing the same nuclide. For example, the  $^{106}\text{Cd}$  ( $n,\gamma$ ) reaction produces the same isotope as a  $^{108}\text{Cd}$  ( $n,2n$ ) reaction which complicates the determination of contributions to the reaction products.
- The activation foil should be optically thin to not cause perturbations of the neutron flux. An additional benefit of relatively thin foils is that the gamma-ray emissions for detection are not significantly attenuated through self-shielding. In general, adding additional foils helps to improve the unfolding results, as long as the entire foil set remains generally optically thin [66].
- The decay nature of the product nuclide should preferably be a gamma-ray emitter. Gamma-ray detection can provide fine energy resolution to determine activation. The discrete gamma-ray emissions provide a means of determining

the source and magnitude of the the foil activation. The energy of the gamma is also of importance. Semiconductor detection methods have a peak intrinsic efficiency near 100 keV with some variance depending on if the semiconductor is p-type or n-type. Beta spectroscopy is also a potential option that may be considered; however, the resolution is not as good as gamma spectroscopy.

## 2.6 Neutron Energy Spectrum Unfolding

Foil activation experiments are a well documented method for determining an incident neutron energy spectrum [64]. The foils are irradiated under a nearly equivalent neutron flux, which serves to activate the foil samples through nuclear reaction channels, each of the which has a unique response function with respect to the neutron flux. The nuclear data and activities of the foils can be used to unfold the incident neutron energy spectrum.

In an ideal situation, the number of foil reactions ( $i$ ) would be selected based on the number of energy groups ( $j$ ) required, and the problem would be formulated as [59, 66]

$$A_i = \sum_{j=1}^N \Sigma_i(E_j) \Phi(E_j) V, \quad i = 1..m \quad (18)$$

In practice, this formulation of the unfolding problem is not used as it often provides nonphysical results. The issue is caused by the varying shapes of reaction cross-sections, which create a poorly constructed matrix and a limit on the number of foils that can be used at a time to prevent changing the neutron flux. There are many methods that aim to provide solutions to the generally degenerate neutron spectrum.

A few examples unfolding methods include matrix inversion, least-squares spectral adjustment, and stochastic algorithms [67]. Direct matrix inversion was previously discussed in the setup of the unfolding problem. Matrix inversion is generally seen

as “ill-posed” and can lead to non-physical results, such as negative fluxes [66, 67]. Stochastic methods rely on random sampling to derive a best-fit or average over a group of reasonably well-fitting spectra [67]. The least-squares method minimizes the chi-square based on a guess spectrum, activation information, and nuclear data [68]. The least-squares method is also known as spectral adjustment and can incorporate more information, most notably the underlying energy dependent nuclear data, into the determination of the resultant spectrum [68].

The general formulation of the least-squares method is derived from minimizing the activation results to the nuclear data and input spectrum [68]. The chi-square ( $\chi^2$ ) is given as per degrees of freedom ( $\nu$ ) as a function of the uncertainty, activation rates, nuclear data, and measured results. The  $\chi^2$  formulation of the least-squares approach can be reduced if there is no time dependency of the neutron flux as

$$\frac{\chi^2}{\nu} = \frac{1}{\nu} \sum_{i=1}^m \frac{(\sum_{j=1}^N \Sigma_i(E_j) \Phi(E_j) - \frac{A_i}{V_{Foil}})^2}{\sigma_i^2} . \quad (19)$$

Providing an initial spectrum is generally required for the unfolding methods. The activities produced for the foils is often highly degenerate, where an infinite amount of spectra could provide the same observable end-point. The initial spectrum allows for the insertion of more physics based results into the unfold. For neutron spectra, an initial guess spectrum is often created with a particle transport code or a deterministic solution. Alternatively, an initial spectrum could be selected from published results, where in some applications provide similar results [69].

### 3. Methodology

Figure 18 displays the overarching research approach. First, the objectives and constraints that provided the ETA design are outlined. Next, the radiation transport simulations for MCNP and SCALE are discussed along with sampling from the nuclear data covariance data for the SCALE Sampler runs. The activation foil pack and neutron flux unfolding methodology is then provided in the context of the data available from the radiation transport calculations. Additionally, the fission product isotope and mass chain models are provided. Finally, the statistical analysis tests utilized throughout the results are discussed to interpret the results.

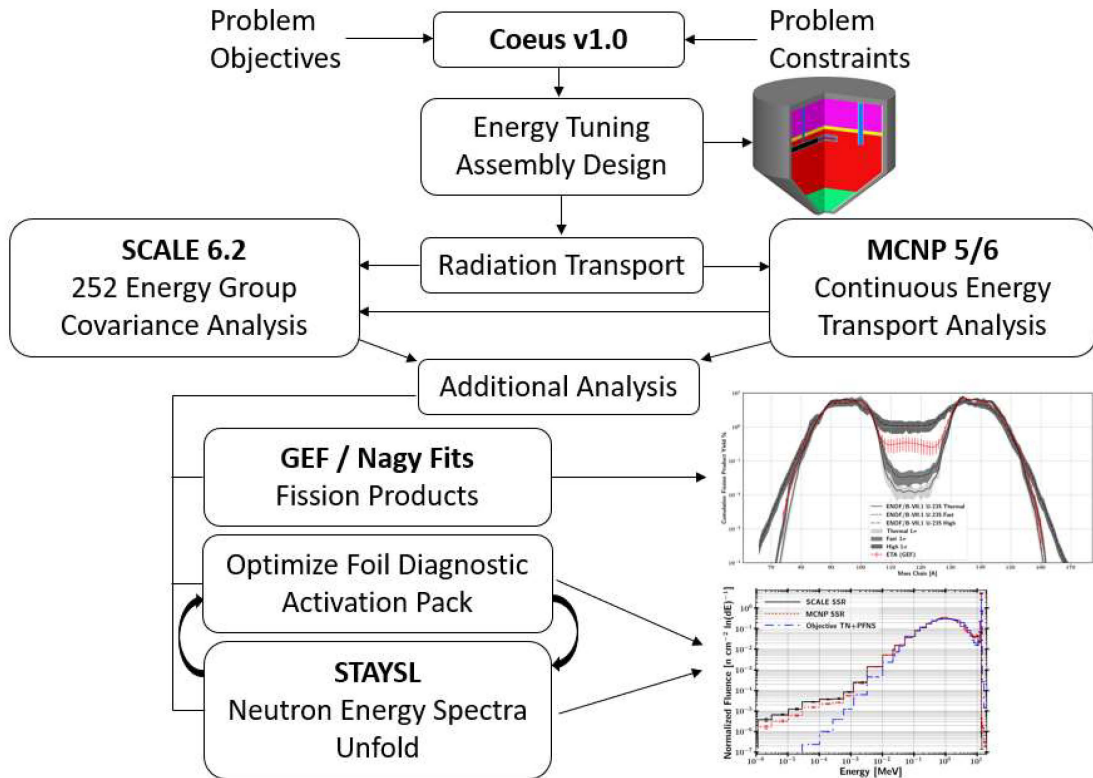


**Figure 18. Overview of the major research components from ETA design to key analysis areas.**

### 3.1 Energy Tuning Assembly Design

The ETA analyzed in this research was taken as an initial condition; however, it is important to understand the motivation that went into the design. Each of the objectives and constraints have impacts on the ability of ETA to effectively shape the neutron source to a TN+PFNS.

The TN+PFNS was created utilizing the Godiva bare critical assembly, a metallic sphere of HEU, to approximate the down-scattered components from the TN and PFNS source neutrons. A Watt fission spectrum volume source and a 14.1 MeV centered point source at a 10 keV plasma temperature were transported through Godiva using MCNP6 [4, 70]. The Godiva transmitted components combined to generate the TN+PFNS with 15% fusion born neutrons and 85% Watt fission neutrons. The objective spectrum was created with the 46 group DPLUS structure, which is utilized in radiation shielding problems and in the DABL69 library [4, 71].

#### 3.1.1 NIF Constraints

There were a few limits to the constraints imposed by NIF that do not directly affect the analysis performed in this study but did affect the ETA design and the spectral shaping capability and fission product production. The three main constraints were a weight limit, stay-out angle, and distance from the DT source, all of which are linked together to form the experimental envelop available for the designed ETA.

The first constraint was a maximum weight of 75 kg. The weight limit lowers the ability of ETA to match the objective spectrum by decreasing the scope of design possibilities and mass available to modify the spectrum. The weight constraint was derived based on the limits of the diagnostic and instrument manipulator (DIM) planned to field ETA at the NIF. The closest standoff range was 15 cm from the DT source mounted on the target positioner (TARPOS) given the allowable weight.

Finally, the stay-out angle provides the laser paths a clear line of sight from the beam ports to the DT capsule. A diagram of the planned ETA experiment is shown in Figure 19. Since the original design, the experiment has been moved to target and diagnostic manipulator (TANDM) 90-124, which provides opportunities to re-evaluate the overall constraints due to increase lift capacity.

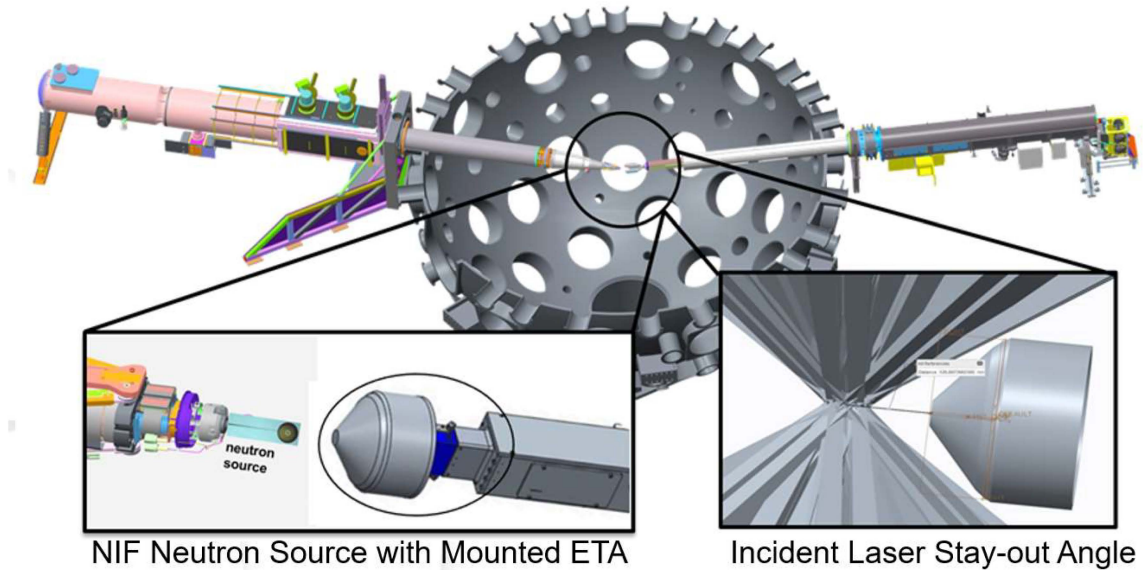


**Figure 19.** Diagram of ETA experiment at the NIF showing ETA installed on TANDM 90-124 with neutron source mounted on TARPOS 90-239. The bottom left graphic shows a notional mounting of ETA on TANDM 90-124. The bottom right graphic highlights the laser path clearance requirement constraint.

### 3.1.2 NIF Source

The NIF source used in the original design of ETA was a “high foot” shot at the NIF and is shown in Figure 20. The indirect drive “high foot” source utilized a hohlraum, shown in Figure 21, responsible for the large downscattered source component shown in Figure 20 [72].

However, source development is a continuing process, and direct drive sources with high neutron outputs and a reduced downscattering component have been developed. The current NIF source modeled for this work was a DT Polar Drive Exploding Pusher

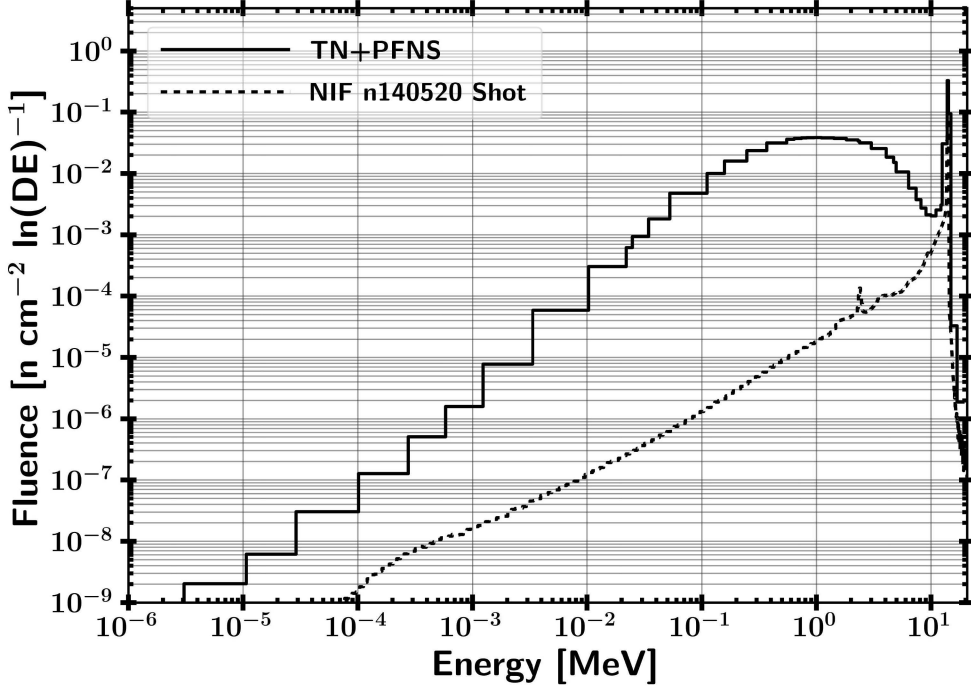


**Figure 20.** Comparison of objective TN+PFNS to NIF source constraint utilizing the 140520 NIF shot.

(PDXP) target with a nominal yield of  $3.7 \times 10^{15}$  neutrons from laser driven inertial confinement fusion. The PDXP source is a DT mixture (65:35 ratio DT) compressed to 8 atmospheres [73]. The capsule is comprised of a hydrocarbon glow discharge polymer (GDP) 2.9 mm in diameter [74]. The PDXP source does not utilize auxiliary systems to achieve compression, unlike other NIF sources that require a hohlraum to smooth out the ablation surface. Instead the compression is driven solely by the NIF laser configuration. The large benefit of using a low mass target is the removal of downscattering within the source hohlraum. This has enabled the PDXP source to be modeled as a 14 MeV point source in previous NIF experiments. The plasma burn width is approximatley 300 ps, so all of the neutrons were modeled as being emitted instantaneously [73].

Many experimental models at NIF utilize a zero-temperature plasma value for the neutron source because the inertial confinement process is not at equilibrium making

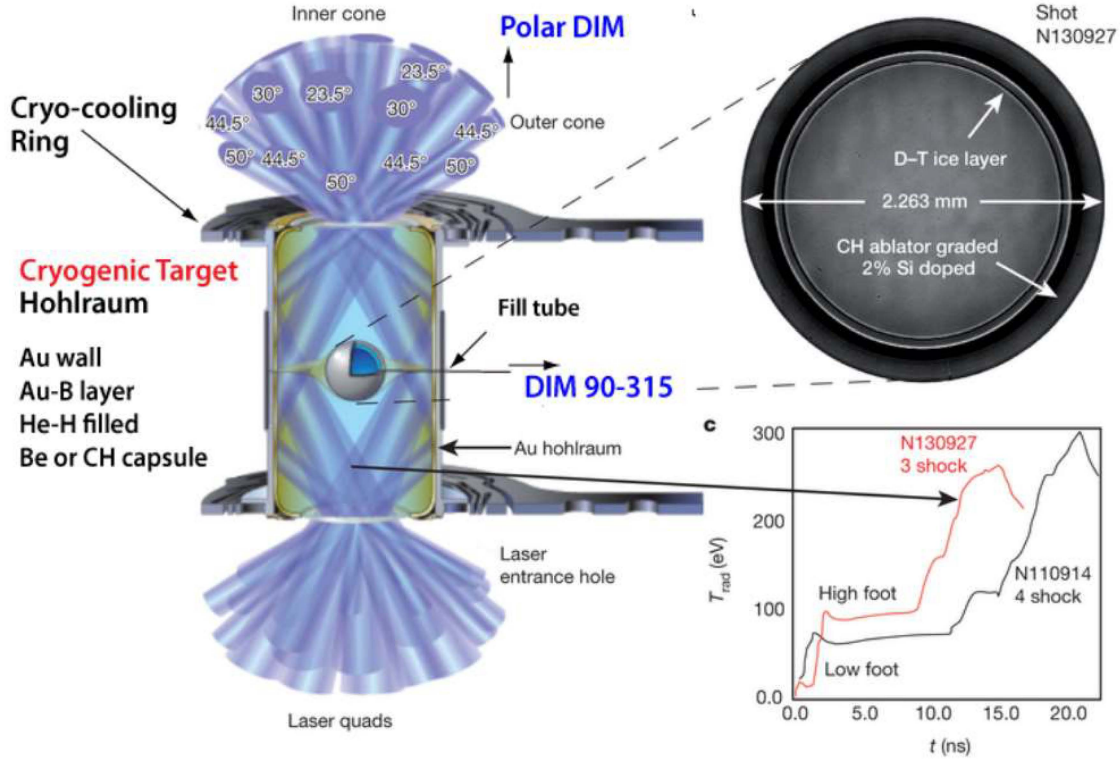


**Figure 21.** NIF shot N130927 utilizing a hohlraum and image of DT source [72]

any temperature value an indirect measurement. These models often use DT neutrons modeled as a 14.03 MeV isotropic point source. However, this is an approximation that neglects the spread in neutron energies due to the plasma temperature.

The plasma temperature from the fusion reaction will result in a distribution of neutron energies due to differences in reaction rates and imparted energy from conservation of mass and energy [75]. The distribution of neutron energies produced by the NIF was taken as a theoretical thermal plasma at a temperature of 10.75 keV [76]. The resultant Gaussian distribution centered at 14.06 MeV has a full width at half maximum of approximately 0.58 MeV. The unnormalized source probability distribution function for the source used in this work is shown in Figure 22.

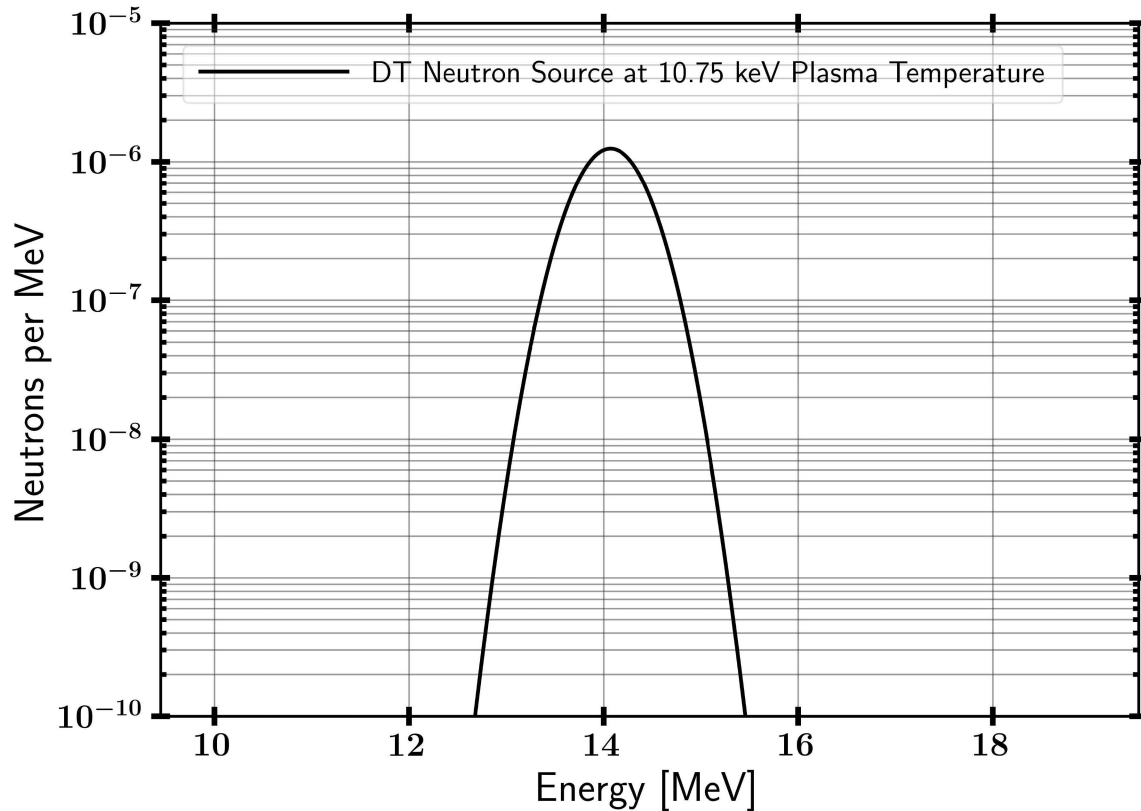


**Figure 22.** 10.75 keV plasma temperature DT fusion source distribution.

### 3.2 Radiation Transport

Three radiation transport simulations were performed to analyze ETA. Both MCNP5 and the SCALE MAVRIC sequence were utilized to increase the degree of confidence in the results. The radiation transport simulations provided results for the reaction rates for foil activation, neutron energy spectra, and temporal aspect of the neutron flux. The modeling efforts and purpose of each code are described in the sections that follow.

#### 3.2.1 Nuclear Data Libraries

A few nuclear data libraries were utilized depending on the application and code system. First, the continuous energy neutron transport simulations performed in

MCNP and SCALE utilized the ENDF/B-VII.1 library [1]. ENDF is a comprehensive nuclear library which contains the data necessary for the transport calculation. ENDF/B-VII.1 was also used for response functions not available in IRDFF or where the IRDFF data was consistent with ENDF. The multi-group nuclear data transport calculations were performed with the 252 group SCALE library based on ENDF/B-VII.1. The 252 group structure is the largest fidelity multi-group SCALE library with samples distributed to utilize in Sampler. The activation foil reactions largely utilized the IRDFF v.1.05 library [50].

It is commonplace for nuclear data libraries to have equivalent information when drawing from the same experimental sources or from each other directly; however, differences do arise in the evaluated data as highlighted in Figure 23. While there is good agreement in the  $^{197}\text{Au}$  ( $n,g$ ) uncertainty, IRDFF had a much larger uncertainty from 1 to 4 keV, and the SCALE 252 group library drops to zero uncertainty after approximately 2.5 MeV. Some of the deviations were based on the group structure utilized.

A few reactions utilized the SCALE ENDF data when the SCALE 252 group data was consistent with the IRDFF or data was not available in the IRDFF. The activation foils and tallied reactions that did not use the IRDFF were  $^{55}\text{Mn}$  ( $n,g$ ),  $^{xxx}\text{U}$  ( $n,f$ ), and  $^{186}\text{W}$  ( $n,g$ ). A comparison between the uncertainties for  $^{55}\text{Mn}(n,g)$  is shown in Figure 24. Overall, there was agreement between the uncertainties. The energy region where the uncertainty has been truncated encompassed a negligible percentage of the reactions, so the impact is minimal.

### 3.2.2 MCNP

A continuous energy radiation transport simulation was performed in MCNP5 in collaboration with the NIF [77]. The NIF model in MCNP5 has been utilized for

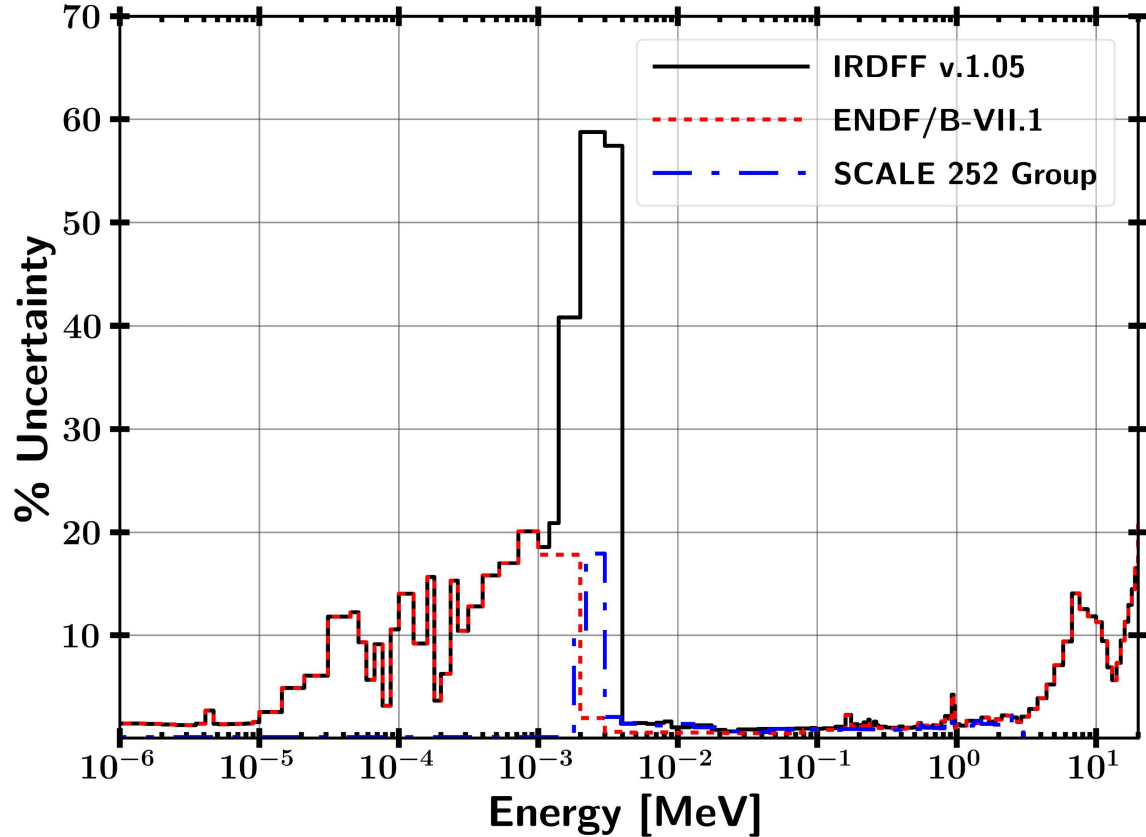


**Figure 23.** Comparison between IRDFF v.1.05, ENDF/B-VII.1, and SCALE 252 Group ENDF/B-VII.1  $^{197}\text{Au}$  (n,g) reaction cross-section uncertainties.

numerous experiments and moving from MCNP to other radiation transport codes is cumbersome due to the high fidelity model that has been built up. ETA was modeled in the full NIF chamber including TARPOS 90-239, TANDM 90-124 with mounted ETA, TANDM 90-348 with diagnostics, the polar DIM, and the first panel walls [78]. The ancillary equipment and surroundings were incorporated into the model to account for ‘room return’ in the NIF chamber. The mean flux at the HEU sample, expected activities of foils, and fission numbers were determined using  $2 \times 10^{11}$  source particles. The variance reduction techniques utilized were the SSR and importance cells.

The MCNP SSR file was used to create sources representing the incident flux from the DT source and room return from supporting equipment. The SSR surfaces were

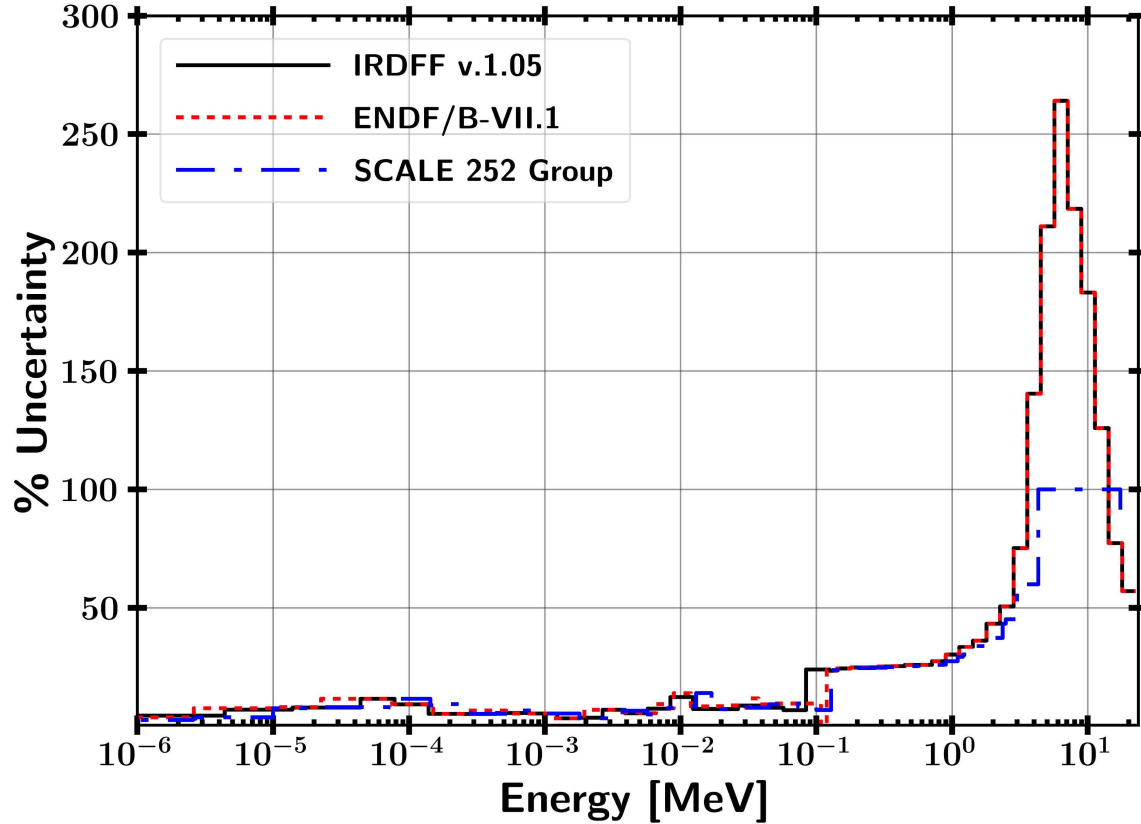


**Figure 24.** Comparison between IRDFF v.1.05, ENDF/B-VII.1, and SCALE 252 Group ENDF/B-VII.1  $^{55}\text{Mn}$  ( $n,g$ ) reaction cross-section uncertainties.

a disk 17.5 cm in diameter at the front (source facing) and bottom of ETA and a connecting cylinder as shown in Figure 25.

The normalized probability distribution functions for the source locations are shown in Figure 26. The impact of the room return in the NIF Chamber is most clearly shown in the cylindrical and back surface. The front facing surface also contains room return; however, the source 14.03 neutrons dominated the spectrum.

The MCNP5 results were used to benchmark the continuous energy solution in MAVRIC. Although it was not feasible to perfectly replicate the source distribution because there are many scattering angles crossing a surface in different directions, it was possible to approximate the behavior for the purpose of quantifying the impact of nuclear data covariance.

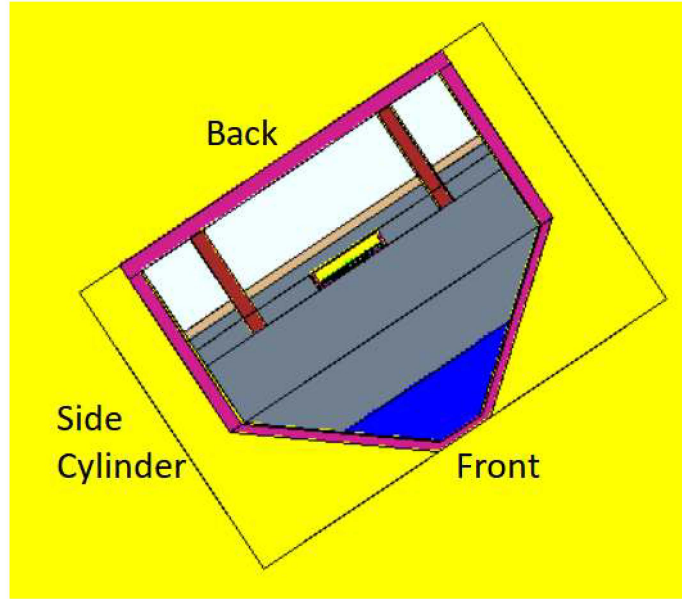


Figure 25. Surfaces for NIF source SSR file. The front source faced the DT point source and the back surface was mounted to TANDM 90-124.

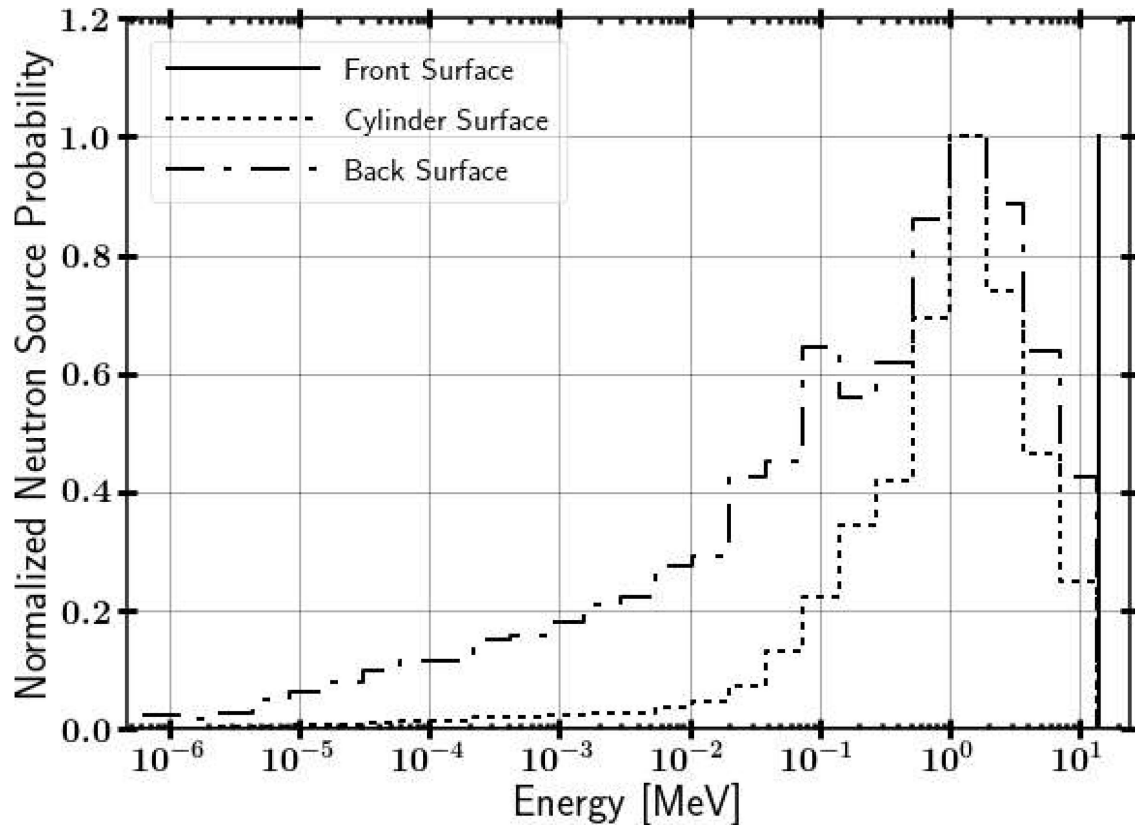


Figure 26. Surfaces source probability distribution functions mapped to SCALE.

### 3.2.3 SCALE MAVRIC

A continuous energy radiation transport simulation was performed in the SCALE MAVRIC sequence which utilizes automated variance reduction techniques along with the traditional Monte Carlo transport calculation. The three SSR sources were mapped over to SCALE by approximating the behavior with source definitions. The total fluence of neutrons passing through the front, back, and cylindrical SSR surfaces were  $6.5 * 10^{14}$ ,  $3.5 * 10^{12}$ , and  $2.4 * 10^{12}$ , respectively. The front source was approximated as a point with the strength determined from the spherical divergence ( $1/R^2$ ) of the source neutrons to the front facing surface. The back source was a disk, and the cylinder was four equal strength line sources facing ETA and emitting in  $2\pi$ . Ideally, the cylindrical source could be mapped over with a cylindrical source; however, the reference directions for emission in SCALE are in Cartesian coordinates.

The benchmarking of the mapping of MCNP to SCALE was performed by comparing the reactions in the foil pack and neutron flux in the HEU foil. Two key aspects were important to determining a goodness of fit. First, the magnitude of the reaction difference between the continuous MCNP and MAVRIC results was nearly equivalent to about 1%. Second, there is not a systematic pattern to the differences between the threshold or thermal reactions modeled in SCALE and MCNP. A comparison between MCNP and SCALE MAVRIC reactions products in the foils and fissions is summarized in Table 1.

The continuous energy SCALE reactions matched fairly well to the MCNP reactions. There was a noted bias of approximately 1% for increasing reactions in SCALE; however, these are within the differences seen in Section 2.4.2. Nonetheless, there were some key deficiencies in the way that the sources were mapped over. First, the SSR source had  $10^9$  sample written points. In MCNP, these points re-sampled at the same entry location on the SSR with new random numbers. For SCALE, the

**Table 1. Activation foil reactions comparison between continuous energy MCNP SSR and SCALE MAVRIC mapped SSR. All statistical uncertainties were below 0.2%.**

Reaction	MCNP SSR Continuous Energy	SCALE MAVRIC Continuous Energy	
	Reactions	Reactions	Percent Change Relative to MCN
$^{90}\text{Zr} (\text{n},2\text{n}) ^{89}\text{Zr}$	1.89E+09	1.91E+09	1.5
$^{58}\text{Ni} (\text{n},2\text{n}) ^{57}\text{Ni}$	1.87E+08	1.90E+08	1.4
$^{58}\text{Ni} (\text{n},\text{p}) ^{58}\text{Co}$	6.54E+09	6.64E+09	1.5
$^{197}\text{Au} (\text{n},2\text{n}) ^{196}\text{Au}$	2.91E+09	2.91E+09	-0.1
$^{197}\text{Au} (\text{n,g}) ^{198}\text{Au}$	1.00E+09	1.02E+09	2.0
$^{115}\text{In} (\text{n,n}') ^{115}\text{In}^{\text{m}1}$	3.81E+09	3.82E+09	0.05
$^{115}\text{In} (\text{n,g}) ^{116}\text{In}^{\text{m}1}$	5.14E+09	5.19E+09	1.0
$^{27}\text{Al} (\text{n,a}) ^{24}\text{Na}$	1.08E+09	1.08E+09	-0.02
$^{186}\text{W} (\text{n,g}) ^{187}\text{W}$	7.21E+08	7.30E+08	1.2
$^{55}\text{Mn} (\text{n,g}) ^{56}\text{Mn}$	3.14E+08	3.23E+08	2.8
$^{235}\text{U}(\text{n,f})$	1.94E+09	1.96E+09	0.5
$^{238}\text{U}(\text{n,f})$	2.70E+07	2.67E+07	-1.1
Total Fissions	1.99E+09	2.00E+09	0.5

impact of the SSR was homogenized over the surface. Also, there was a systematic bias of the room return that was not captured in the source approximations. The ancillary equipment in the room increased the scattering back to ETA in that region. Again, this was homogenized over the entire surface for SCALE. Last, the angular resolution for the SCALE sources was restricted to equal probability in  $2\pi$ ; however, there is undoubtedly a systematic trend that was missed.

Figures 27 and 28 show the relative residual flux on a logarithmic and linear energy scale comparing the MCNP values to the SCALE continuous energy MAVRIC and SCALE 252 group Sampler values. There are three regions of differences between the continuous energy solutions; the 252 group comparison is described in the next section. First, no tallies were captured in SCALE above 14.2 MeV. These events born from HEU fissions were very low probability and do not contribute largely to the result. Second, there is a slight difference between 10 MeV and the prompt DT

peak which is likely caused by the systematic room return that was homogenized.

 at low energy ( $< 1$  keV) there was a larger thermal flux than the MCNP flux which can be attributed to the approximations in source mapping.

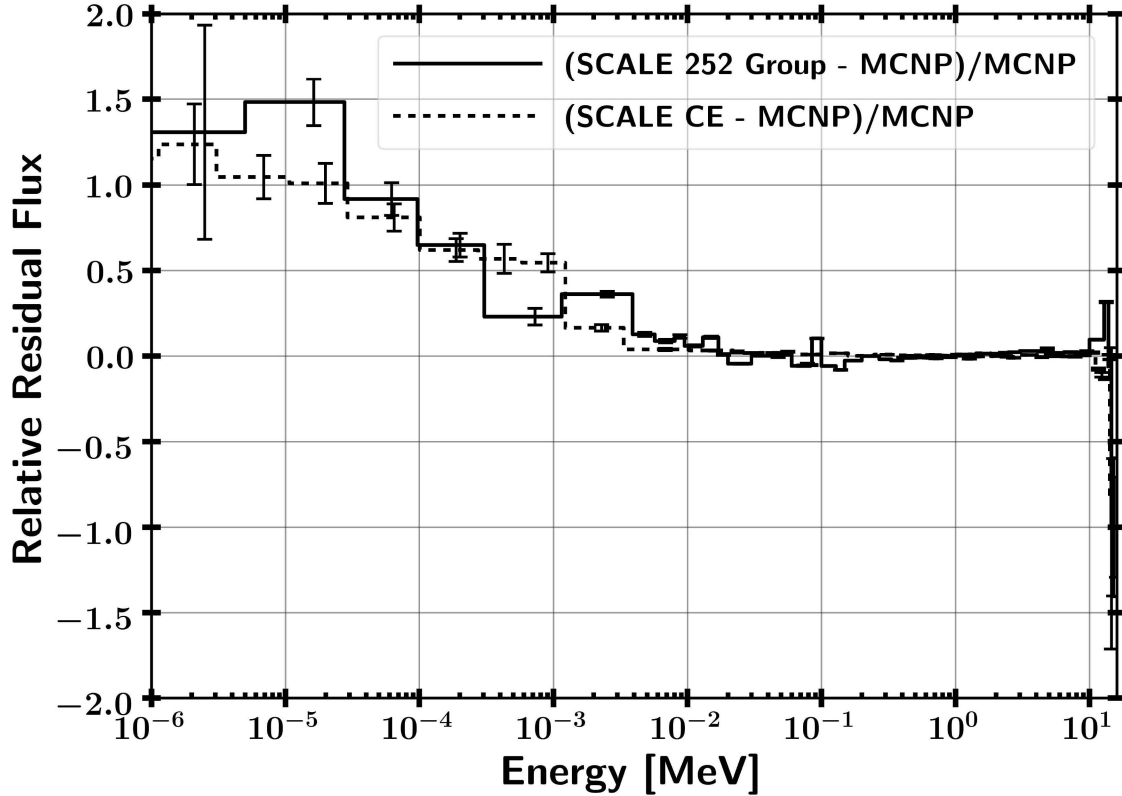


**Figure 27.** Logarithmic energy fluence residuals comparing MCNP, SCALE MAVRIC Continuous Energy (CE), and SCALE 252 group Sampler. The relative residuals tally compared to MCNP values of 0, 1, and -1 indicate agreement, double the flux was tallied and all of the flux was not tallied, respectively.

### 3.2.4 SCALE Sampler Sequence

A 252 group radiation transport simulation was performed for 182 discrete trials in Sampler to build up a distribution of Monte Carlo responses to capture the systematic nuclear data uncertainty. The Sampler sequence is a “super-sequence” that acts as a wrapper above the MAVRIC sequence [58]. The nuclear data libraries were randomly perturbed to determine the distribution of responses due to uncertainty in

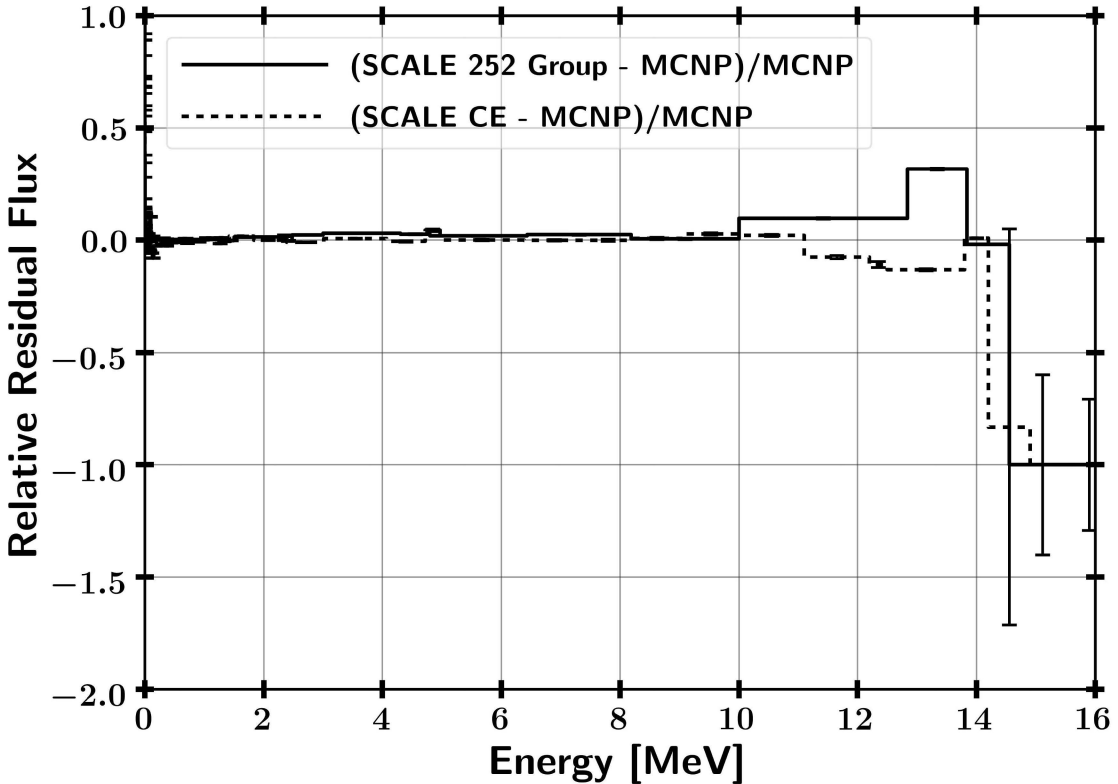


**Figure 28.** Linear energy fluence residuals comparing MCNP, SCALE MAVRIC Continuous Energy (CE), and SCALE 252 group Sampler. The relative residuals tally compared to MCNP values of 0, 1, and -1 indicate agreement, double the flux was tallied and all of the flux was not tallied, respectively.

the transport due to nuclear data.

The SCALE Sampler module enabled analysis of nuclear data covariance. The unperturbed nuclear data was executed for the first sample along with a user-defined number of samples. The sample nuclear data libraries were perturbed nuclear data based on the covariance largely developed from ENDF/B-VII.1; however, additional information has been included from ENDF/B-VI, ENDF/B-VII.2 (proposed at the time), JENDL-4.0, and collaborative research between Brookhaven National Laboratory, Los Alamos National Laboratory, and Oak Ridge National Laboratory. Finally, the nuclear data covariance libraries included information completed in the Working Party on International Nuclear Data Evaluation Cooperation Subgroup-26 [58].

The associated Sampler libraries contained 1,000 pre-sampled neutron cross-sections limited to 56 and 252 group structures. It is important to note the weighting functions for SCALE's library which are a Maxwellian from  $10^{-5}$  eV to 0.1 eV, a Watt Fission spectrum from 80 keV to 10 MeV, and  $1/E$  between 0.1 eV to 80 keV and for 10 to 20 MeV. A notable issue with utilizing a single group structure for all applications is the weighting function to process the continuous energy cross-sections will affect the result flux is dramatically different. This problem is difficult in that a group structure would be needed for each individual problem and is further complicated by changes in the neutron spectra in different regions of a problem.

The continuous energy MAVRIC script was modified by changing the library to the 252 group version and adding the Sampler wrapper to maintain the same inputs. Table 2 presents a comparison between MCNP and SCALE MAVRIC 252 group reactions products in the foils and fissions. There are some important discrepancies that are caused by the 252 group structure. The 252 group Sampler mean total reactions were generally in agreement with the continuous energy solutions with three exceptions:  $^{89}\text{Zr}$ ,  $^{57}\text{Ni}$ , and  $^{56}\text{Mn}$ . The first two threshold reactions were attributed directly to the flux weighting of the 13.8 to 14.6 MeV group utilized, where the nearly all of the reactions take place. The 252 group  $^{55}\text{Mn}$  reaction difference from MCNP was caused by the flux weighting and the bulk of the difference occurs below 80 keV. The 252 group library performed well for the majority of the reactions because many of the activation reactions are saturated by the PFNS, which is synonymous with the Watt Fission neutron spectrum.

Additionally, from Figures 27 and 28, there were notable differences in the multi-group modeled neutron flux spectrum compared to the continuous energy results. First, the neutron population between 10 and 14 MeV was increased as the macroscopic cross-sections for bismuth and tungsten are overestimated in the group wise

**Table 2. Activation foil reactions comparison between continuous energy MCNP SSR and 252 group SCALE MAVRIC mapped SSR. All statistical uncertainties were below 0.2%.**

multirow2*Reaction	MCNP SSR Continuous Energy	SCALE Sampler 252 Group	
	Reactions	Reactions	Percent Change Relative to MCNP
$^{90}\text{Zr}$ (n,2n) $^{89}\text{Zr}$	1.89E+09	2.05E+09	8.6
$^{58}\text{Ni}$ (n,2n) $^{57}\text{Ni}$	1.87E+08	2.20E+08	17.4
$^{58}\text{Ni}$ (n,p) $^{58}\text{Co}$	6.54E+09	6.65E+09	1.5
$^{197}\text{Au}$ (n,2n) $^{196}\text{Au}$	2.91E+09	2.93E+09	0.6
$^{197}\text{Au}$ (n,g) $^{198}\text{Au}$	1.00E+09	9.92E+08	-0.8
$^{115}\text{In}$ (n,n') $^{115}\text{In}^{\text{m}1}$	3.81E+09	3.86E+09	1.2
$^{115}\text{In}$ (n,g) $^{116}\text{In}^{\text{m}1}$	5.14E+09	5.14E+09	-0.1
$^{27}\text{Al}$ (n,a) $^{24}\text{Na}$	1.08E+09	1.06E+09	-1.1
$^{186}\text{W}$ (n,g) $^{187}\text{W}$	7.21E+08	7.09E+08	-1.8
$^{55}\text{Mn}$ (n,g) $^{56}\text{Mn}$	3.14E+08	2.64E+08	-15.9
$^{235}\text{U}(n, f)$	1.94E+09	1.95E+09	0.01
$^{238}\text{U}(n, f)$	2.70E+07	2.70E+07	0.03
Total Fissions	1.99E+09	1.99E+09	0.004

cross-section. While there was similar behavior to the continuous energy solution at low energy, the multi-group approach was also slightly increased compared to MCNP due to the increased reactions at high energy.

Sampler was performed for 182 trials until the responses converged to a solution to build up the distribution of responses to use for random sampling and bootstrapping. Figure 29 displays the convergence of the mean and uncertainty of the bootstrapped values for a few selected reactions. The  $^{55}\text{Mn}$  (n,g) was the least converged and largest relative error reaction due to high systematic uncertainty and relatively large nuclear data uncertainty over the ETA spectrum.

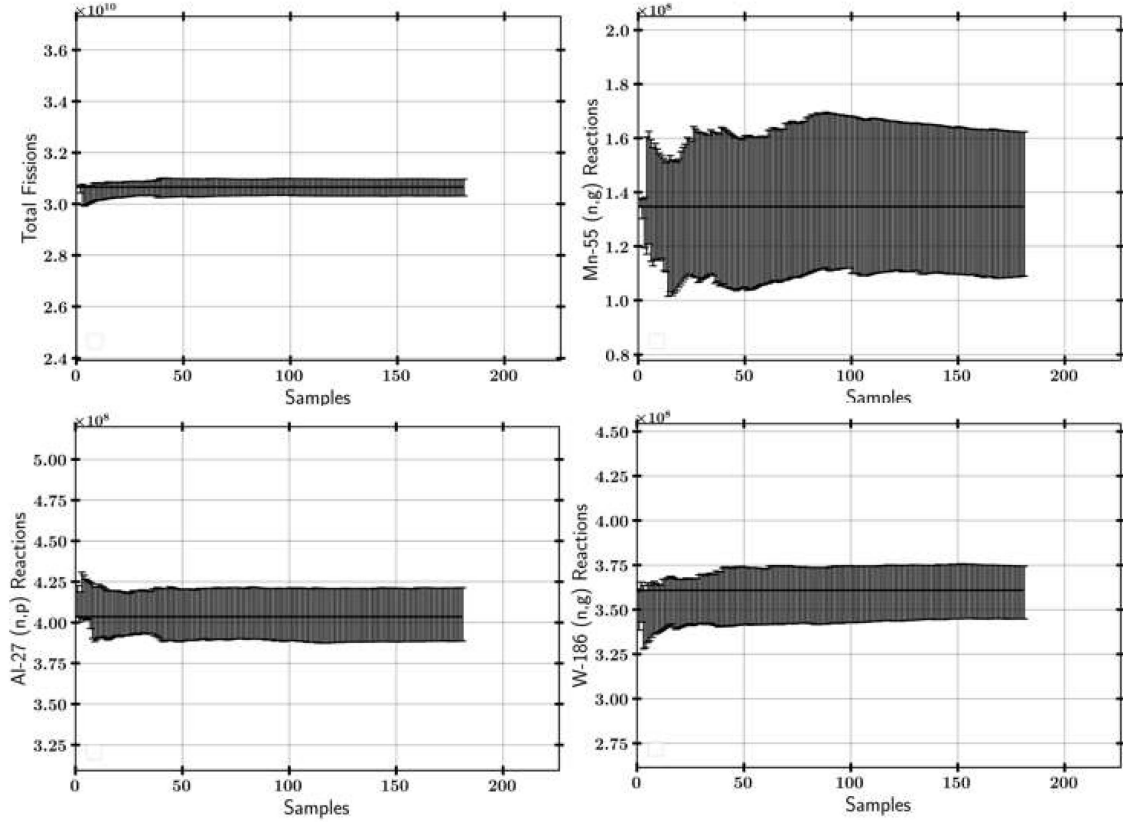


**Figure 29.**  $U(n,f)$ ,  $^{55}Mn$  ( $n,g$ ),  $^{27}Al$  ( $n,p$ ), and  $^{186}W$  ( $n,g$ ) sampled histogram and reaction convergence as a function of Sampler trial. The convergence graphs included the IRDFF nuclear data covariance.

### 3.3 Nuclear Data Covariance

Capturing the full nuclear data uncertainty is essential because it is often a dominant unknown in nuclear applications [79]. The majority of uncertainty analysis done to date focus on integrated quantities such as the effective criticality of a nuclear reactor [80] [81]. However, applications such as radionuclide production rely on a single reaction channel that is observed, which can have much larger uncertainties than noted in integral quantities. Furthermore, it is important to note that ENDF based uncertainties may also be underestimates of the general nuclear data uncertainty [48].

The methodology to incorporate the IRDFF nuclear data in the SCALE Sampler module is shown in Figure 30. There are three key contributions to the uncertainty of

a result in this radiation transport simulation. First, the uncertainty in the neutron transport was quantified using the SCALE Sampler module. Second, the uncertainty in the reaction cross-section was assessed using IRDFF data. In most uncertainty quantification analysis, these two nuclear data systematic uncertainties ( $\sigma_{sys}$ ) are treated at the same time. However, these were separated in this analysis to incorporate the IRDFF reactions and uncertainty. Last, every Monte Carlo based result has statistical uncertainty  $\sigma_{stat}$ , which can be driven to negligible values with enough computation resources.

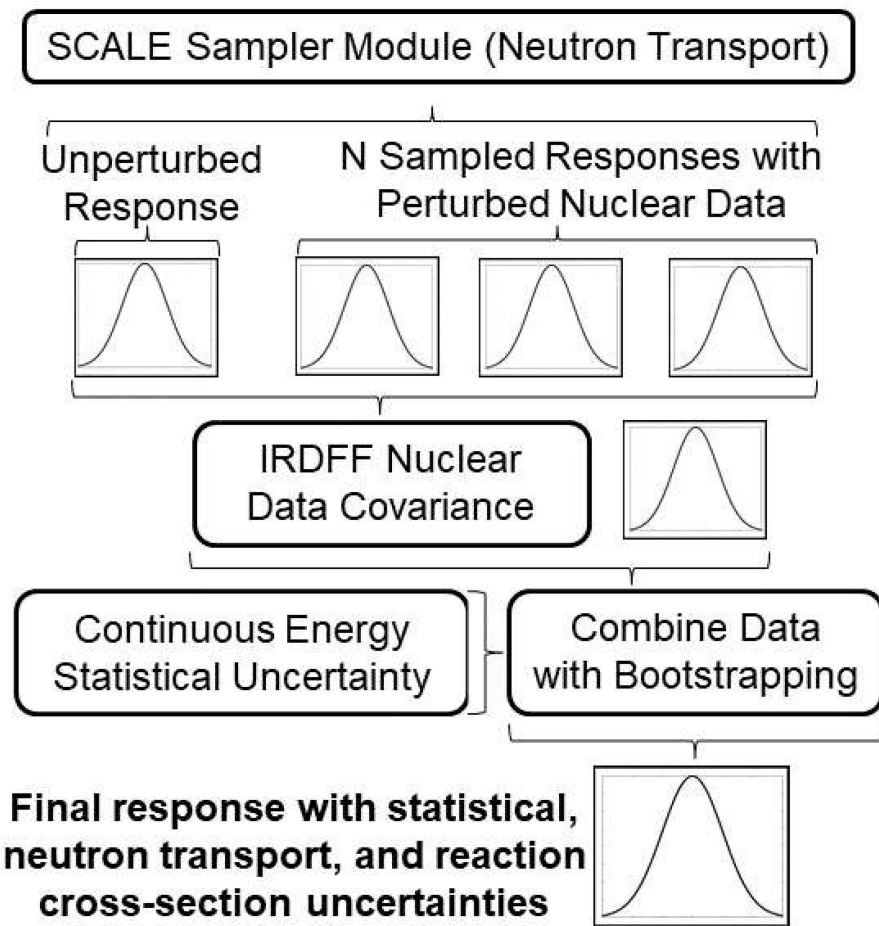


**Figure 30.** Methodology flowchart to insert nuclear data uncertainty for reaction channel from alternative library into SCALE.

### 3.3.1 Sampling Transport Related Uncertainties

The SCALE Sampler module was utilized to assess the neutron transport response uncertainty by generating independent samples to characterize the distribution of responses. The transport related uncertainties are quantified in the neutron fluence on the HEU and activation foils. For each trial, Sampler utilized a different set of nuclear data to transport the source neutrons through the geometry. The variance in the energy dependent fluence over the trials determined the transport related uncertainties. One benefit of the 252 group structure utilized by SCALE was that the uncertainty in the reaction rates follow linearly from the fluence so better statistics at low energy are easier to achieve in comparison with a continuous energy solution.

### 3.3.2 Sampling Nuclear Data Covariance Libraries

There were options to perturb a variable inside of Sampler; however, there were presently no methods to include correlations to allow for a user defined response function in Sampler (i.e. IRDFF cross-section) to be sampled with a covariance matrix. Instead the reaction rate response was calculated independently of the Sampler runs assuming that the nuclear data follows a correlated multivariate normal distribution utilized by the SCALE Sampler sequence [82] [57] [83] [58]. The nuclear cross-sections were converted to a 252 group format in SCALE, while the uncertainties were converted from the IRDFF format by linear interpolation of the midpoint bin energies. The linear interpolation was used to approximate the uncertainty when the bin structure did not align with the mapped energy group structure, which was deemed appropriate due to the uncertainty varying linearly over small energy ranges.

The nuclear data and uncertainty were sampled from the multivariate normal distribution for each independent Sampler trial. The reaction tally ( $R$ ) result was perturbed by the ratio of the macroscopic cross-sections ( $\Sigma$ ) before and after multi-

variate random sampling to create group-wise perturbation parameters ( $Q$ ) with the neutron flux ( $\phi$ ) over 252 groups (g).

$$R = \sum_{g=1}^{252} \phi_g \Sigma_g Q_g \quad (20)$$

The net result effectively modified the microscopic cross-section to form the perturbed  $R$ . The multivariate normal distribution sampled data acted as a set of constants that are multiplied to each energy group [83].

### 3.3.3 The Case for Sampling with Alternative Probability Distribution Functions

As stated, common practices for stochastic sampling approaches are built around the multivariate normal distribution which has a very straightforward way to sample from nuclear data covariance matrices. The log-normal distribution and normal distribution produce similar approximations for small relative uncertainties; however, the distribution functions behave differently with large variance. The log-normal functional form also is more appropriate for physical properties that cannot take on negative values such as **neutron** cross-sections which can have uncertainties greater than 100%. The  $^{55}\text{Mn}$  (n,g) reaction for example has large uncertainty at higher neutron energies. The evaluated data and experimental data informing the (n,g) reaction cross-section near 14 MeV in ENDF/B-VII.1 is shown in Fig. 31.

The experimental data is spread over an order of magnitude and most dense around the evaluated cross-section which supports the use of a log-normal distribution over the normal distribution. The sampling of the nuclear data covariance matrices with log-normal distribution with equivalent expectation values and spread of values to a normal distribution can produce drastically different results in radiation transport results.

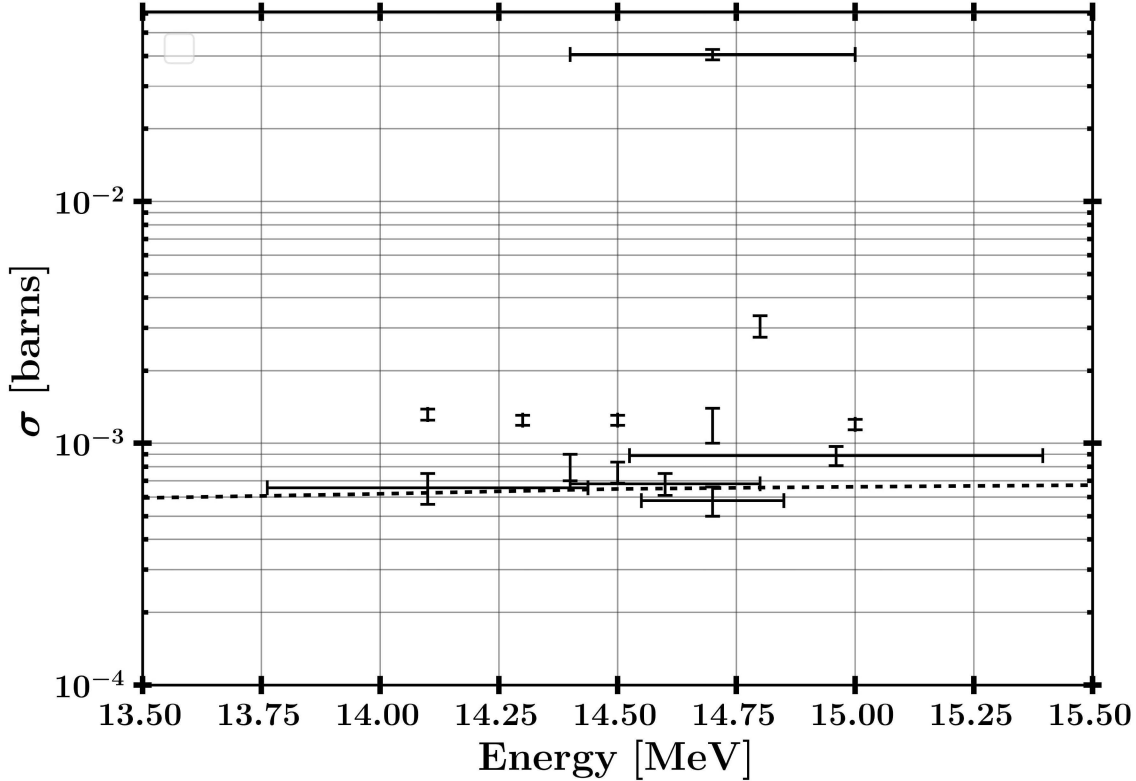
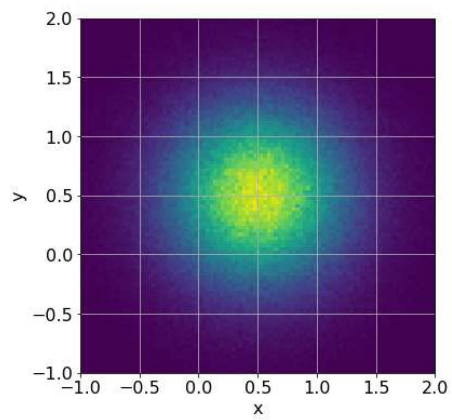


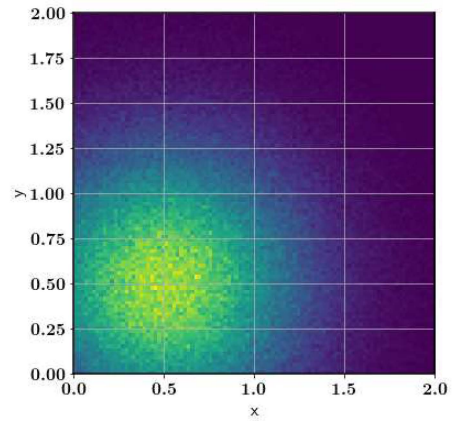
Figure 31. Experimental nuclear data informing  $^{55}\text{Mn}$  (n,g) reaction in comparison with the evaluated nuclear data contained in ENDF/B-VII.1. [1]

To illustrate why a log-normal or similar distribution may be more appropriate, a Monte Carlo simulation was conducted simulating darts thrown on a board with a mean value in the x and y Cartesian coordinates of 0.5. This example assumes negative values are a non-physical quantity. Three distributions were compared over varying uncertainty, a normal distribution, and normal distribution with negative numbers rejected as with multivariate normal distribution approach and a log-normal distribution. The mean dart position on the board and mean radius from the mean dart position were compared, and the outcome is shown in Table 3. The distribution of darts is shown in Figure 32.

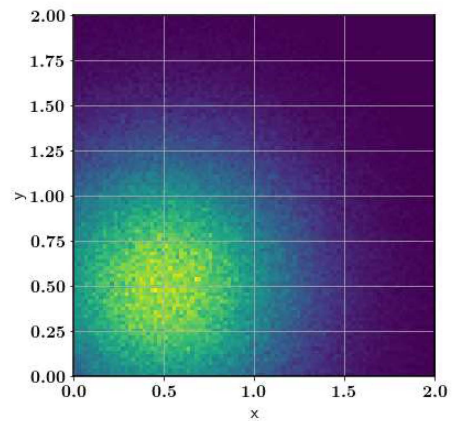
There were important aspects of the outcomes in the very simplistic example. First, all distributions performed well at low uncertainty which was expected given that a log-normal and normal distribution are close approximations in this range.



(a) Normal Distribution



(b) Normal Distribution with Negatives Rejected



(c) Log-normal Distribution

**Figure 32.** Normal, normal with rejected negatives, and log-normal distribution of darts in example Monte Carlo simulation.

**Table 3.** Monte Carlo Darts results with normally, normally with rejected negative values, and a log-normal distribution.

Distribution	Normal	Normal Rejected	Log-normal
$\mu = 0.5 \sigma = 0.5$			
$\bar{x}$ and $\bar{y}$	$0.5 \pm 0.5$	$0.64 \pm 0.4$	$0.5 \pm 0.5$
$\bar{r}$	$0.63 \pm 0.32$	$0.50 \pm 0.25$	$0.51 \pm 0.49$
$\mu = 0.5 \sigma = 0.25$			
$\bar{x}$ and $\bar{y}$	$0.5 \pm 0.25$	$0.51 \pm 0.24$	$0.5 \pm 0.25$
$\bar{r}$	$0.31 \pm 0.16$	$0.29 \pm 0.15$	$0.29 \pm 0.19$
$\mu = 0.5 \sigma = 0.05$			
$\bar{x}$ and $\bar{y}$	$0.5 \pm 0.05$	$0.5 \pm 0.05$	$0.5 \pm 0.05$
$\bar{r}$	$0.06 \pm 0.03$	$0.06 \pm 0.03$	$0.06 \pm 0.03$

This shows that a normal distribution is a good approximation for stochastic sampling radiation transport codes for materials with low relative uncertainties. At large uncertainty, where negative values are drawn often, there were many differences that impact the results of sampling. The normal and log-normal distributions predicted the mean Cartesian coordinate values well. However, the range of radii from the points were different as the underlying distributions behaved differently at large uncertainty as the log-normal distribution most probable value is lower value but has a larger likelihood of sampling relatively large numbers. The negative value removed normal distribution overestimated the mean value as more emphasis was placed on the larger numbers. Manipulations could have been made to weight lesser valued non-negative samples to create a better fitting solution; however, this would still not be completely representative of the normal distribution. In any case, sampling from a normal distribution was not the optimal solution when the uncertainty in the data was large. The neutron transport uncertainties are and sampling method are fortunately somewhat mitigated in that uncertainties are generally larger in regions where the reaction cross-section are lower, so the net result on the problem may be lower.

The methodology for Sampling the nuclear data libraries utilized the multivari-

ate normal distribution to stay consistent with Sampler and the other versions of stochastic sampling methods noted. It is important to understand the implications of utilizing each sampling method. The impact to this research is that the true nuclear data uncertainty may not be fully achievable, but rather an estimation of the uncertainty is determined.

### 3.3.4 Statistical Bootstrapping of Sampler Results

The results of each of the perturbed nuclear data samples were combined using statistical bootstrapping. Bootstrapping is a method to determine uncertainty in a given dataset by using random sampling with replacement. The bootstrapped values are equivalent to a Gaussian distribution if the underlying data is Gaussian in shape. However, bootstrapping is most useful to use here if a distribution of responses does not follow a Gaussian distribution.

SCALE contained functionality to automatically perform some of this work; however, the addition of IRDFF covariance to the responses made it necessary to develop a set of Python 2.7 functions to process the data. First, a sample is randomly selected from the  $n$  samples in the dataset. The “0” sample contained the unperturbed nuclear data result, while the 1 through  $n$  samples have perturbed nuclear data. Next, the 252-group energy structure was collapsed into a smaller group size to reduce  $\sigma_{stat}$  uncertainty in the lower energy bins. Finally, the value and the relative uncertainty associated with the response were used to sample from a Gaussian distribution to include the statistical error from that trial. The process was repeated to 10,000 times, with replacement to provide under 0.1% convergence of the bootstrapped value relative error. The final value and relative uncertainty are used as the final result, which includes  $\sigma_{stat}$  and  $\sigma_{sys}$ .

### 3.3.5 Mapping Nuclear Data Systematic Error to Alternate Group Structures

One important approximation that must be made for group-wise cross-section uncertainty models is that the uncertainty is not largely dependent on the group-structure. A study benchmarking nuclear data uncertainty between two methods showed that the integral uncertainty is relatively insensitive to the group structure utilized [82]. Additionally, there is uncertainty in published uncertainties making any small differences found between alternate group structures potentially negligible.

#### Case Study

A test case for the  $^{58}\text{Ni}$  ( $n,2n$ ) reaction was performed to outline the impact of the weighting function and group structure on uncertainty results. The  $^{58}\text{Ni}$  ( $n,2n$ ) reaction in ENDF was linear in energy and in cross-section which enabled straightforward analytical solutions. The cross-sections from ENDF/B-VII.1 available in SCALE are shown in Figure 33 along with the SCALE relative uncertainty of the reaction cross-section.

The test case utilized a normalized flux integral of  $1 \text{ ncm}^{-2}s^{-1}$  from the threshold energy of 12.4 MeV up to 20 MeV with the flux bin weighted by the bin widths. The flux profile was chosen to eliminate bias from the energy bin shapes for the 252 group structure. The test flux is shown in Figure 34.

The 252 group structure underestimated  $R$  compared to the continuous energy solution by 0.4% for the test case. More importantly, the reaction uncertainty differed by 0.2%, which suggested that uncertainties may differ from the continuous energy solution by approximately the same magnitude as  $R$ . This conclusion presents an issue of determining the uncertainties when the group structure produces results that are significantly different. The implication for this research means that the  $^{89}\text{Zr}$ ,  $^{57}\text{Ni}$ ,

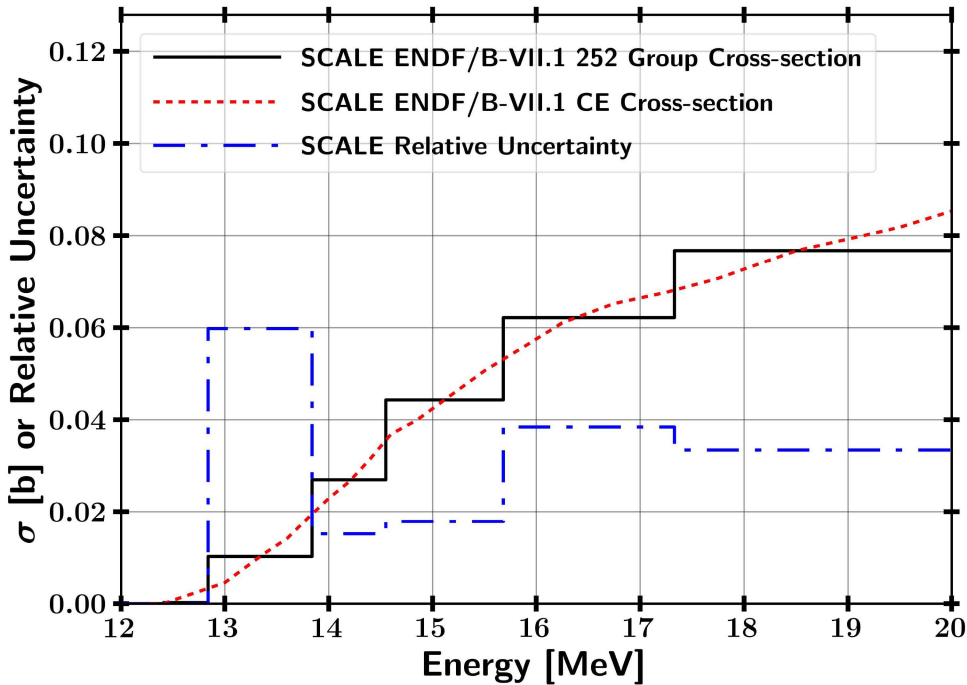


Figure 33. Comparison between  $^{58}\text{Ni}$  ( $n,2n$ ) continuous energy (CE) and 252 group 1/E weighted cross-sections. The relative uncertainty of the reaction cross-section is shown.

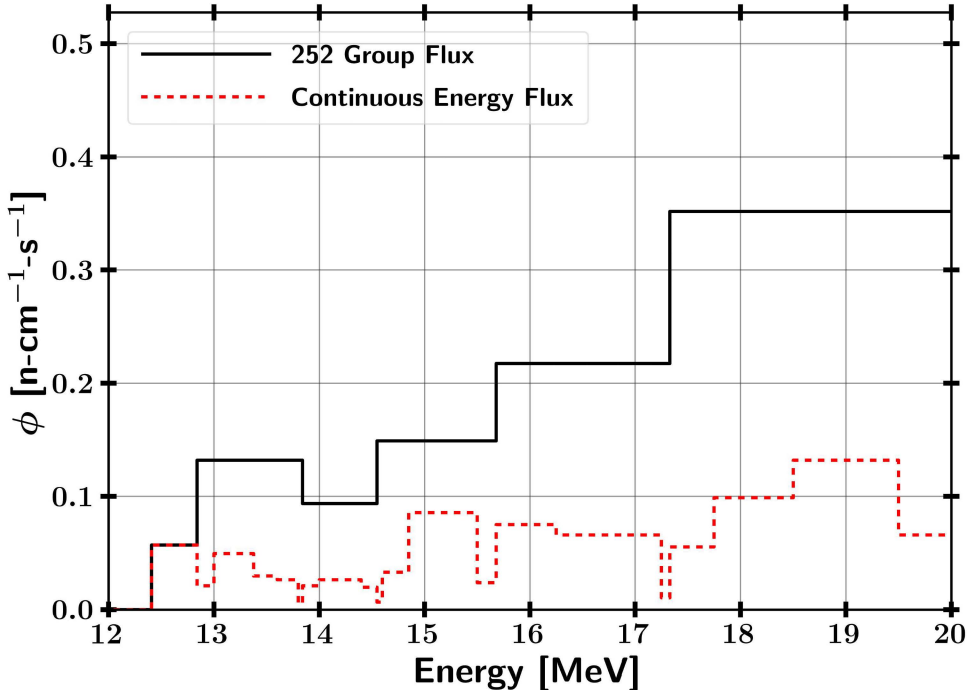


Figure 34.  $^{58}\text{Ni}$  ( $n,2n$ ) case study constant differential flux.

and  $^{56}\text{Mn}$  reaction uncertainties can vary by approximately 10-20% of their nominal value.

### Integral Data

The total reaction uncertainty was determined by the uncertainty in the bootstrapped 252 group value. The integral uncertainty was used with the mean value from the continuous energy solution. It is important to note that the uncertainty in this uncertainty is on the order for which the group wise transport analysis misrepresents the continuous energy solution based on the previous section.

### Differential Data

The differential uncertainties were treated as being a function of energy through linear interpolation of the midpoint bin energies. This approach provides an approximation of the total uncertainty for the target bin structures. The 252 group structure results were assumed to be a combination of  $\sigma_{stat}$  and  $\sigma_{sys}$  through quadrature. The 252 groups were collapsed at low energy to create a 66 group structure.

$$\sigma_{total} = \sqrt{\sigma_{sys}^2 + \sigma_{stat}^2} \quad (21)$$

Thereby  $\sigma_{sys}$  was determined for each group. The reverse treatment was performed to add in  $\sigma_{sys}$  to the target group structure.

## 3.4 Activation Foil Pack and Neutron Energy Spectra Unfold

### 3.4.1 Activation Foils Selection

A study concluded, based on the energy groups ranging from 0.01 eV to 18 MeV, that Au, As, Cd, In, Ir, Er, Mn, Ni, Se, Sm, W, and Zn were suitable to fully cover the

neutron energy spectrum [6]. In addition to this identified set, the ETA experiment will have a large amount of high energy neutron flux necessitating the use of additional high energy foils. Unfortunately, the experimental cavity in the ETA will not have enough space to fit all of these foils.

The foil pack designed to be placed in the ETA experimental cavity was created to be able to successfully unfold the incident neutron spectra from the activation foils. The activation foils were selected with many important factors including the cross-section, gamma emission, and half life as discussed in Section 2.5.2. However, the most notable aspects were the confidence in the nuclear data, the inclusion in the IRDFF database, and energy range that the foils are activated. The final set of foils, containing Zr, Ni, Au, In, Al, W, and Mn, was analyzed for the this study. The relevant nuclear data and foil thicknesses for each selected foil are summarized in Table 4.

**Table 4. Activation foils selected for ETA experiment to be utilized to unfold the neutron energy spectrum. Each reaction has well documented nuclear data and is available within the IRDFF utilized by STAYSL.**

Foil (Thickness)	Reaction	Threshold [MeV] (@ 10 mb)	Decay Radiation [keV] (Intensity)	$T_{1/2}$
Zr (1 mm)	$^{90}\text{Zr}(\text{n},2\text{n})^{89}\text{Zr}$	12.1 (12.1)	909.2 (0.9904)	78.41 hrs
Ni (1 mm)	$^{58}\text{Ni}(\text{n},2\text{n})^{57}\text{Ni}$	12.4 (13.3)	1,378 (0.817)	35.6 hrs
	$^{58}\text{Ni}(\text{n},\text{p})^{58}\text{Co}$	0 (1.3)	810.8 (0.9945)	70.86 days
Au (0.1 mm)	$^{197}\text{Au}(\text{n},2\text{n})^{196}\text{Au}$	8.1 (8.3)	355.7 (0.87)	6.17 days
	$^{197}\text{Au}(\text{n},\text{g})^{198}\text{Au}$	Thermal	411.8 (0.9562)	2.69 days
In (1 mm)	$^{115}\text{In}(\text{n},\text{n}')^{115}\text{In}^{\text{m}1}$	0.336 (0.597)	336.24 (0.459)	4.49 hrs
	$^{115}\text{In}(\text{n},\text{g})^{116}\text{In}^{\text{m}1}$	Thermal	1293.56 (0.848)	54.29 min
Al (1 mm)	$^{27}\text{Al}(\text{n},\text{a})^{24}\text{Na}$	3.25 (6.7)	1368.63 (0.9999)	15 hrs
W (1 mm)	$^{186}\text{W}(\text{n},\text{g})^{187}\text{W}$	Thermal	685.51 (0.332)	24 hrs
Mn (1 mm)	$^{55}\text{Mn}(\text{n},\text{g})^{56}\text{Mn}$	Thermal	846.8 (0.9885)	2.58 hrs

Many additional foils were considered for the experiment; however, they were not utilized for various reasons:

- Cd, Cu - Multiple reaction channels contribute to produce the same activation products
- Nb, Eu, Dy, Sm, Se, Er, Ir - Large nuclear data uncertainty in activation region
- Zn -  $^{64}\text{Zn}$  (n,p) nearly equivalent to Aluminum reaction
- Sc, As, Co, Nb - Low activity at 2 hours (small cross-section, too long of half-life, too short of half-life)
- Fe - Low abundance of activation isotope of interest

### 3.4.2 Neutron Flux Unfolding with STAYSL

The modeled foil activities were used with the underlying nuclear data to unfold the neutron spectrum using STAYSL. STAYSL determines the incident neutron flux using a generalized least-squares spectral adjustment based on a  $\chi^2$  comparison of the measured activities and the activities calculated from an adjusted flux [35]. STAYSL utilizes data from the IRDFF v1.05 library because of the increased level of benchmarking for dosimetry applications.

Additionally, STAYSL required an initial guess spectrum. The activities produced for the foils is often degenerate, where an infinite amount of spectra could provide the same end-point. The initial spectrum allowed for the insertion of more physics to guide the overall result. The initial guess spectrum utilized the MCNP-calculated neutron fluence in the HEU foil with  $\sigma_{sys}$  mapped from the Sampler results to the 129 group STAYSL form<sup>a</sup>

STAYSL had several modules that are used to unfold the neutron spectrum from the calculated activities. The main components used in this analysis are SHIELD, SIG-PHI Calculator, and PNNL STAYSL. The Beam Correction factor was not used because the NIF irradiation time is much less than the half-lives of the reaction

products. SHIELD was used to generate energy dependent neutron self-shielding factors for non-threshold reactions. SHIELD was not used on high energy threshold reactions because there is negligible shielding. The SIG-PHI Calculator was used to consolidate all of the reaction information and generate gamma-ray self-shielding factors. The STAYSL input decks were created from these modules and the modified MCNP spectrum. The cross-section library utilized was the 129 group IRDFF v.1.05 library.

STAYSL utilizes activity information ( $A^\circ$ ), a neutron flux, a nuclear data matrix ( $P$ ), and covariance matrices in the formulation of the  $\chi^2$  statistic. The  $\chi^2$  is minimized based on the activity information ( $\bar{A}$ ) and neutron flux and nuclear data parameters ( $\bar{P}$ ). The  $\chi^2$  statistic utilized in STAYSL is given by [68];

$$\chi^2 = \begin{bmatrix} P - \bar{P} \\ A^\circ - \bar{A} \end{bmatrix}^\dagger \bullet \begin{bmatrix} N_P & 0 \\ 0 & N_{A^\circ} \end{bmatrix}^{-1} \bullet \begin{bmatrix} P - \bar{P} \\ A^\circ - \bar{A} \end{bmatrix} \quad (22)$$

where  $N_P$  is the covariance matrix from the flux and nuclear data and  $N_{A^\circ}$  is the activity covariance matrix. However, the STAYSL  $\chi^2$  has a possibility to go negative as the activities are not directly squared. The  $\chi^2$  statistic presented in Chapter 4 neglect uncertainty in the neutron fluence which would otherwise be incorporated into STAYSL  $\chi^2$  results.

The sensitivity of the activation foil pack unfolding was assessed by unfolding the spectrum for each of the sets of activation data available from the Sampler results. STAYSL was executed on each trial to build up a set of  $\chi^2$  and unfolded neutron fluence responses. Each set of activation products produces a test point which contained the reaction products produced under the same neutron fluence but varying activation cross-sections. The incident fluence on the foils was the only correlated value for each reaction trial. The activation cross-sections contained no correlations between

foils. The unfolding process contained a mix of increases and decreases between varied reactions.

### 3.5 Fission Product Isotopes

Three key aspects were important for the selection of individual fission products for this study. First, data must exist in order to estimate the fission product production. Second, the radioactive decay characteristics or radiochemical analysis techniques must exist to determine the relative production. A consideration for radiochemical analysis is that all of the gaseous fission products will be lost in the dissolution. Last, the fission products were selected to sample from key regions of the fission product distribution.

The fission products yields were normalized to a single, peak fission product. Using relative activities and production can increase the  statistics of the experimental results and remove some detection biasing.  $^{95}\text{Zr}$  was chosen to compute the relative activities of the other fission products, and Table 5 outlines the fission products used for the experiment analysis. It is important to note that some isotopes will require other forms of detection such as beta spectroscopy, not through gamma-ray spectroscopy.  $^{112}\text{Pd}$  and  $^{161}\text{Tb}$  for example have low energy gammas and may not be expected to be detected using a high purity germanium detector. 

#### 3.5.1 GEF

GEF utilizes a combination of Monte Carlo, theory, and experimental data to determine fission observables, such as fission products [33]. GEF is applicable over a wide array of fissioning systems including isotopes with a atomic number from 80 to 112 [84]. The underlying model has been shown to have good predictive power, albeit with relatively large uncertainties, using potential energy surfaces of the fission

**Table 5. Selected fission products for analysis of the NIF experiment**

A	FP	Location	T <sub>1/2</sub>	E <sub>γ</sub> [keV]	BR <sub>γ</sub> %
91	<sup>91</sup> Sr	Light Peak	9.65 hrs	1024.3	33.5
92	<sup>92</sup> Sr	Light Peak	2.66 hrs	1383.93	90
95	<sup>95</sup> Zr	Light Peak	64.032 days	756.725	54.38
97	<sup>97</sup> Zr	Light Peak	16.749 hrs	743.36	93.09
99	<sup>99</sup> Mo	Light Peak	65.976 hrs	739.5	12.2
103	<sup>103</sup> Ru	Light Peak	39.247 days	497.085	91
105	<sup>105</sup> Ru	Valley	4.44 hrs	724.3	47.3
109	<sup>109</sup> Pd	Valley	13.7012 hrs	88.03	3.67
111	<sup>111</sup> Ag	Valley	7.45 days	342.13	6.7
112	<sup>112</sup> Pd	Valley	21.04 hrs	18.5	27
113	<sup>113</sup> Ag	Valley	5.37 hrs	298.6	10
115	<sup>115g</sup> Cd	Valley	53.46 hrs	527.901	27.4
132	<sup>132</sup> Te	Heavy Peak	3.204 days	772.6	77.9
140	<sup>140</sup> Ba	Heavy Peak	12.7527 days	537.3	24.39
141	<sup>141</sup> Ce	Heavy Peak	32.511 days	145.4	48.29
143	<sup>143</sup> Ce	Heavy Peak	33.039 hrs	293.3	42.8
144	<sup>144</sup> Ce	Heavy Peak	284.91 days	133.5	11.09
147	<sup>147</sup> Nd	Heavy Wing	10.98 days	531	13.4
149	<sup>149</sup> Pm	Heavy Wing	35.08 hrs	385.95	3.1
151	<sup>151</sup> Pm	Heavy Wing	28.4 hrs	340.08	22.5
153	<sup>153</sup> Sm	Heavy Wing	46.284 hrs	103.2	29.25
156	<sup>156</sup> Eu	Heavy Wing	15.19 days	1153.8	11.5
161	<sup>161</sup> Tb	Heavy Wing	6.89 days	25.65	23.2

barrier of the fissioning system, theory, and adjustments based on empirical parameters [42]. GEF incorporates covariance information, multi-chance fission, and many other unique capabilities. Depending on the fissioning system, there are approximately 50 parameters that have been fit to align with experimental results.

The values for the chain yield distribution calculated by GEF were determined utilizing separate calculations for each energy group defined by the midpoint bin energy of the fissioning system, <sup>236</sup>U for neutron induced <sup>235</sup>U fission. The uncertainty was

determined using a combination of the GEF Monte Carlo statistical and systematic uncertainty and the systematic uncertainty from the Sampler results.

### 3.5.2 Nagy Fits for Fission Product Isotopes

Experimental data published from the 1960s to 2016 was fit to Equation 4 through a least squares minimization [1,34,85–92]. Multi-chance fission was taken into account by fitting the fission products in the symmetric region with one fit up to 5.5 MeV and a second fit above. The asymmetric fission isotopes were fit with one equation over the entire energy range.

The uncertainty in the experimental measurements was taken into account by modifying the data consistent with the experimental uncertainty. Each energy data point was sampled according to the mean and uncertainty assuming a normal distribution. One thousand Monte Carlo'd fist were performed for each isotope to provide convergence of approximately 0.1%. The neutron fluence uncertainty was added in quadrature to the fission product production calculated by convolving the fits to experimental yield with the neutron energy spectrum. The final value reflects the total yield expected with the systematic nuclear data, statistical simulation, and experimental uncertainties.

### 3.5.3 Systematic Uncertainties

Systematic uncertainties, if known, were propagated with the error propagation formula given as

$$\sigma_q = \sqrt{(\frac{\partial q}{\partial x}\sigma_x)^2 + (\frac{\partial q}{\partial y}\sigma_y)^2 + (\frac{\partial q}{\partial z}\sigma_z)^2 + \dots} \quad (23)$$

The the propagation of uncertainty for a function ( $q(x, y, z, \dots)$ ) is the square root of the sum of squared uncertainty, ( $\sigma_x$ ), of the variables, ( $x, y, z, \dots$ ) multiplied by the

partial derivative of the function with respect to that variable [93].

Geometric systematic uncertainty based on the positioning of the ETA, DT capsule, or components of ETA has the possibility to introduce systematic uncertainty. The NIF facility has rigid tolerances for positioning systems. It is assumed that the geometric uncertainty of this type is negligible.

A related uncertainty that may arise is the configuration of the NIF chamber. The planned configuration may not be the exact experiment performed, which ultimately may require that this analysis is repeated post-experiment if large perturbations are seen. An example of a possible change is the addition of another experiment in the NIF target chamber. A first order assessment tested spheres of aluminum and lead simulating other experiments nearby showed that the total number of fissions for 2019 experiment can deviate by a few percent for medium to high Z experiments similar in size to ETA. Few experiments in the NIF chamber are as massive as the ETA, but all material in the chamber can cause backscattering and impact the solution to some degree.

Another source of systematic uncertainty is the neutron source itself, which is difficult to characterize completely. The source strength of the NIF is a potentially large contribution to error from the expected results. However, this is an experimentally measurable quantity, and any increase or decrease in the number of source neutrons will produce a linear response in all of the data presented in this work. Therefore, the uncertainty in the source strength is not a large concern.

A scoping study was performed to analyze the impact of the source energy distribution on the results. The results are discussed further in Chapter 4; however, it is important to understand to what extent the source may impact the solution. A 14.03 MeV point source which was used for this work was compared to a 10.75 keV plasma temperature Albe derived point source centered at 14.06 MeV, a 14.06

MeV point source, the full NIF transported MCNP SSR, and the SCALE continuous energy results with the MCNP SSR mapped. The results for the comparison are shown in Figure 35.

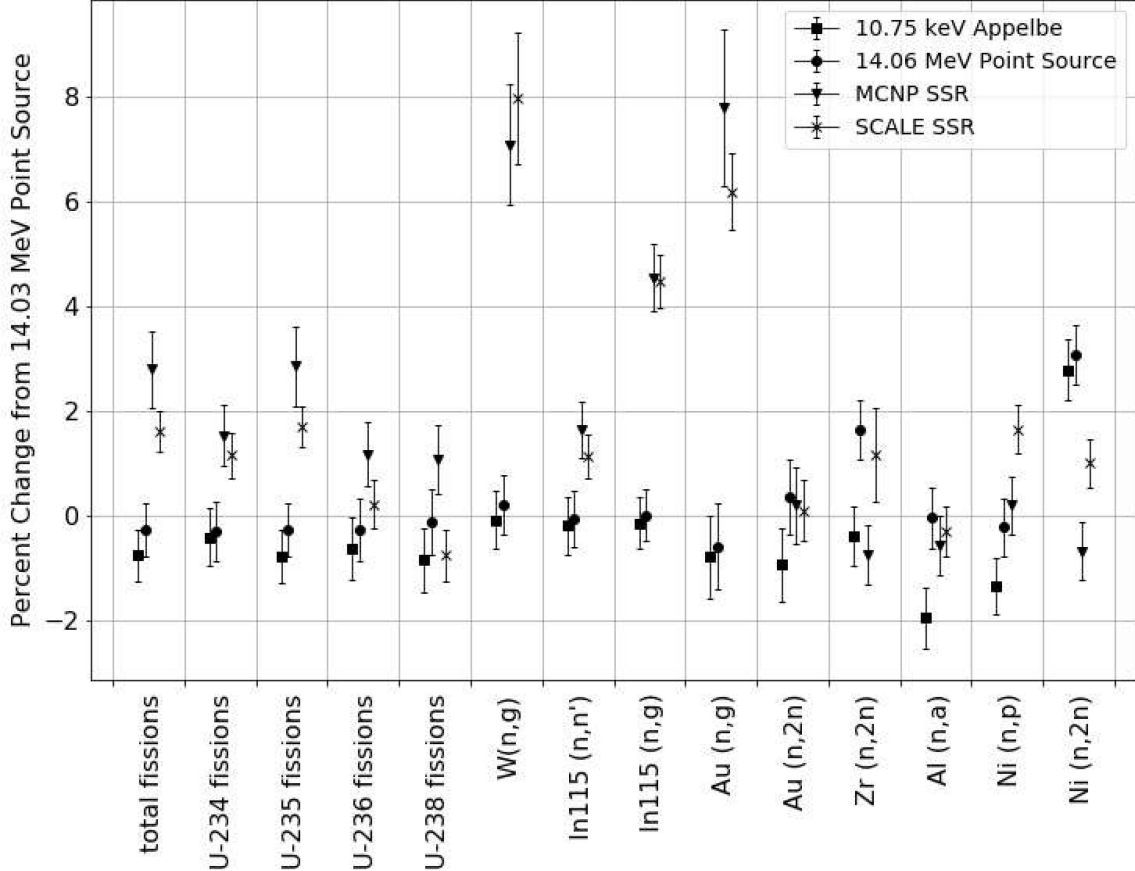


**Figure 35. Comparison of results based on NIF source term.** The statistical uncertainties of the underlying datasets are all less than 1%. Utilizing a higher energy source term provides larger production of threshold reactions while including the room return increases the thermal reactions.

The comparison highlight a few key details that impact the solution set as a function of source neutron energy and inclusion of the room return. First, source distributions containing higher energy neutrons (Appelbe or 14.06 MeV) impacted the threshold reactions by as much as 2%. This is due to increasing cross-section for the threshold reactions at higher energy. Second, the thermal reactions increased substantially by including the room return and scattering back from the DIM. The

down-scattered neutrons have lower energy and contributed more to the total response for these non-threshold reactions. Last, the comparison between MCNP and SCALE SSR results was generally consistent. The deviations from the mean were not systematically distributed as highlighted in Table 1.

### 3.6 Statistical Analysis Tests

The statistical tests utilized for this research include the Chi-square statistic, Pearson correlation coefficient, and the Kolmogorov-Smirnov (K-S) statistic. The Chi-square is primarily utilized to test categorical distributions to assess if the results were governed by the expected distribution. The Pearson correlation coefficient and KS statistic both provide information regarding the similarity of two distributions.

1. Chi-square Statistic The chi-square statistic ( $\chi^2$ ) is a useful tool for the interpretation of categorical results to expected values. The reduced  $\chi^2$ , as used in the foil activation neutron flux unfolding, is [93]

$$\frac{\chi^2}{\nu} = \frac{1}{\nu} \sum_{i=1}^n \left( \frac{\text{observed value} - \text{expected value}}{\text{observed standard deviation}} \right)^2 \quad (24)$$

The degrees of freedom are defined with the observed data points and parameters computed to fit the equation. The degrees of freedom is the number of measurements in one data set minus one for the case of comparing two data sets of equal size.

The  $\chi^2/\nu$  can be used to assess goodness of fit between two distributions. The expected value for  $\chi^2/\nu$  is unity if the calculated distribution is described by the expected distribution.  $\chi^2/\nu$  much greater than one indicate that there is indeed a difference between the expected distribution and the observed.

The null hypothesis for the  $\chi^2$  statistic is that the two sets of data are governed from the expected distribution. The test of independence shows the probability of rejecting this null hypothesis. The p-value can be used to compare the results of the expected distribution to the calculated  $\chi^2/\nu$ . The p-value is the probability of finding a larger  $\chi^2/\nu$ , given the calculated result. A small p-value ( $<0.05$ ) signifies there is a strong significance level for the results not being governed by the expected distribution. P-values above the cutoff significance level fail to reject the null-hypothesis. A p-value of 0.05 or greater is generally accepted as statistically significant; however, this can change depending on the field of study.

## 2. Pearson Correlation Coefficient

The Pearson correlation coefficient provides a measure of the linear relationship between two sets of data. This metric is often used for comparative signal analysis. Like the  $\chi^2$  statistic, the Pearson correlation coefficient is best suited to normally distributed data. Additionally, the statistic is meant for linear datasets, so a non-linear function correlation may be misrepresented. The formula for the Pearson correlation coefficient is given as a function of “n” data points for two distributions defined by points  $x_i$  and  $y_i$  as:

$$r = \frac{n \sum x_i y_i - (\sum x_i)(\sum y_i)}{\sqrt{n \sum x_i^2 - (\sum x_i)^2} \sqrt{n \sum y_i^2 - (\sum y_i)^2}} \quad (25)$$

The null hypothesis of this statistic is that there is no correlation between the two datasets. The p-value indicates the probability of an uncorrelated system producing a correlation coefficient at least as large in magnitude. Small p-values ( $<0.05$ ) indicate a statistically significant Pearson correlation coefficient.

## 3. Kolmogorov-Smirnov (K-S) statistic

The K-S two-sample statistic compares the cumulative distribution functions (CDF) between two sets of data. The K-S statistic provides information on the relative magnitude of the distributions, so it is useful in combination with the Pearson correlation coefficient to quantify the similarity between two distributions. The K-S statistic is given as a function of the supremum (maximum) between the expected and observed CDF as shown in Equation 26. The null hypothesis for this test is that the two samples are drawn from the same distribution. Unlike the other statistical tests shown earlier, a large p-value ( $> 0.05$ ) from the K-S statistic fails to reject the null hypothesis.

$$D = \sup_x |CDF_{exp}(x) - CDF_{obs}(x)| \quad (26)$$